

# NAVAL POSTGRADUATE SCHOOL Monterey, California

2

AD-A245 804



## THESIS

DTIC  
ELECTR  
FEB 10 1992  
S B D

DYNAMIC RESPONSE OF CYLINDRICAL SHELLS TO  
UNDERWATER END-ON EXPLOSION

by

Luis A. Boticario

DECEMBER 1991

Thesis Advisor:

Young W. Kwon

Approved for public release: Distribution is unlimited

92-03062



92 2 051

REPORT DOCUMENTATION PAGE				Form Approved OMB No 0704-0188	
1a. REPORT SECURITY CLASSIFICATION Unclassified		1b. RESTRICTIVE MARKINGS			
2a. SECURITY CLASSIFICATION AUTHORITY		3. DISTRIBUTION/AVAILABILITY OF REPORT Approved for public release: Distribution is unlimited			
2b. DECLASSIFICATION/DOWNGRADING SCHEDULE					
4. PERFORMING ORGANIZATION REPORT NUMBER(S)		5. MONITORING ORGANIZATION REPORT NUMBER(S)			
6a. NAME OF PERFORMING ORGANIZATION Naval Postgraduate School		6b. OFFICE SYMBOL (If applicable) ME	7a. NAME OF MONITORING ORGANIZATION Naval Postgraduate School		
6c. ADDRESS (City, State and ZIP Code) Monterey, CA 93943-5000		7b. ADDRESS (City, State, and ZIP Code) Monterey, CA 93943-5000			
8a. NAME OF FUNDING/SPONSORING ORGANIZATION		8b. OFFICE SYMBOL (If applicable)	9. PROCUREMENT INSTRUMENT IDENTIFICATION NUMBER		
8c. ADDRESS (City, State, and ZIP Code)		10. SOURCE OF FUNDING NUMBER			
		PROGRAM ELEMENT NO	PROJECT NO	TASK NO	WORK UNIT ACCESSION NO.
11. TITLE (Include Security Classification) DYNAMIC RESPONSE OF CYLINDRICAL SHELLS TO UNDERWATER END-ON EXPLOSION					
12. PERSONAL AUTHORS LUIS A. BOTICARIO					
13a. TYPE OF REPORT Master's Thesis		13b. TIME COVERED FROM _____ TO _____	14. DATE OF REPORT (Year, Month, Day) DECEMBER 1991		15. PAGE COUNT 84
16. SUPPLEMENTARY NOTATION The views expressed are those of the author and do not reflect the official policy or position of the Department of Defense or the U.S. Government					
17. COSATI CODES			18. SUBJECT TERMS (Continue on reverse if necessary and identify by block numbers)		
FIELD	GROUP	SUB-GROUP	underwater shock		
19. ABSTRACT (Continue on reverse if necessary and identify by block numbers) Both numerical and experimental analyses were performed to investigate underwater shock propagation and the induced nonlinear response of cylindrical shells with end caps. The cylinders were subjected to shocks from explosive charges at 12 inches (near-field) and 28 feet (far-field) from the cylinder. An underwater shock test was also performed with the far-field explosion. The numerical results were compared with the experimental data. Stresses and strains occurring in the structure as well as the pressure in the water were studied. The far-field explosion caused the largest circumferential deformations close to both end plates and an accordion oscillatory motion of the cylindrical shell. The near-field explosion caused severe plastic deformation in the neighborhood of the closest end plate to the charge. The stiffeners had, as expected, a larger effect on the circumferential stresses than on the longitudinal stresses. The measured and calculated strains agreed well qualitatively near the remote end plate from the charge.					
20. DISTRIBUTION AVAILABILITY OF ABSTRACT <input checked="" type="checkbox"/> UNCLASSIFIED/UNLIMITED <input type="checkbox"/> SAME AS RPT <input type="checkbox"/> DTIC USERS			21. ABSTRACT SECURITY CLASSIFICATION unclassified		
22a. NAME OF RESPONSIBLE INDIVIDUAL Young W. Kwon		22b. TELEPHONE (Include Area Code) (408) 646-3385		22c. OFFICE SYMBOL ME/Kw	

Approved for public release: Distribution is unlimited  
Dynamic Response of Cylindrical Shells to Underwater End-On  
Explosion

by

Luis A. Boticario  
Lieutenant, United States Navy  
B.S., University of Michigan, 1986

Submitted in partial fulfillment of the  
requirements for the degree of

MASTER OF SCIENCE  
IN MECHANICAL ENGINEERING

from the

NAVAL POSTGRADUATE SCHOOL

DECEMBER 1991

Author:

  
Luis A. Boticario

Approved by:

  
Young W. Kwon, Thesis Advisor

  
Young S. Shin, Second Reader

  
A.J. Healey, Chairman  
Department of Mechanical Engineering

**ABSTRACT**

Both numerical and experimental analyses were performed to investigate underwater shock propagation and the induced nonlinear response of cylindrical shells with end caps. The cylinders were subjected to shocks from explosive charges at 12 inches (near-field) and 28 feet (far-field) from the cylinder. An underwater shock test was also performed with the far-field explosion. The numerical results were compared with the experimental data. Stresses and strains occurring in the structure as well as the pressure in the water were studied. The far-field explosion caused the largest circumferential deformations close to both end plates and an accordion oscillatory motion of the cylindrical shell. The near-field explosion caused severe plastic deformation in the neighborhood of the closest end plate to the charge. The stiffeners had, as expected, a larger effect on the circumferential stresses than on the longitudinal stresses. The measured and calculated strains agreed well qualitatively near the remote end plate from the charge.



<b>Accession For</b>	
NTIS GRA&I	<input checked="" type="checkbox"/>
DTIC TAB	<input type="checkbox"/>
Unannounced	<input type="checkbox"/>
Justification _____	
By _____	
Distribution/	
<b>Availability Codes</b>	
Dist	Avail and/or Special
A-1	

## TABLE OF CONTENTS

I.	INTRODUCTION . . . . .	1
II.	ANALYSIS AND EXPERIMENT . . . . .	3
	A. NUMERICAL ANALYSIS . . . . .	3
	B. NUMERICAL MODELLING . . . . .	6
	C. UNDERWATER EXPLOSION TEST . . . . .	14
III.	RESULTS AND DISCUSSIONS . . . . .	23
	A. NUMERICAL RESULTS OF FAR-FIELD EXPLOSION . .	23
	B. COMPARISON BETWEEN NUMERICAL AND EXPERIMENTAL RESULTS . . . . .	36
	C. NUMERICAL RESULTS OF NEAR-FIELD EXPLOSION . .	45
	1. Pressure Wave Study . . . . .	51
	2. Ring Stiffener Study . . . . .	51
IV.	CONCLUSIONS . . . . .	65
	APPENDIX: UNIAXIAL TENSION TEST DATA FOR 6061-T6 ALUMINUM . . . . .	68
	LIST OF REFERENCES . . . . .	72
	INITIAL DISTRIBUTION LIST . . . . .	74

## LIST OF FIGURES

Figure 2.1.	Finite Element Meshes for Near-Field Explosion . . . . .	9
Figure 2.2.	Stiffened Cylinders with End Plates . .	10
Figure 2.3.	Finite element meshes of a cylinder subject to a far-field explosion . . . .	12
Figure 2.4.	Finite element discretization over 4 inch span at one end of cylinder . . . .	13
Figure 2.5.	Cylinder and Crane Rigging . . . . .	16
Figure 2.6.	Test Geometry at the Surface . . . . .	17
Figure 2.7.	Test Geometry (Ranges in Feet) . . . . .	18
Figure 2.8.	Water Plume from Shot . . . . .	19
Figure 2.9.	Cylinder Geometry . . . . .	20
Figure 3.1.	Deformation Time Histories . . . . .	24
Figure 3.1.	(cont). Deformation Time Histories . . .	25
Figure 3.1.	(cont.) Deformation Time Histories . . .	26
Figure 3.2.	Axial Velocities of Nodes at Both End Plates of Cylinder . . . . .	28
Figure 3.3	Locations for Strain Computation . . . .	30
Figure 3.4	Circumferential Strains Close to End Plates . . . . .	31
Figure 3.5.	Circumferential Strain 20.75 Inches from the Closest End Plate to the Explosive Charge . . . . .	33
Figure 3.6.	Longitudinal Strains in the Vicinity of the Closest End Plate to the Explosive Charge . . . . .	35
Figure 3.7.	Longitudinal Strains 37.5 Inches from the Closest End Plate, of Different Densities, to the Explosive Charge . . .	37
Figure 3.8.	Circumferential Strains 20.75 Inches from the Closest End Plate, of Different Densities, to the Explosive Charge . . . . .	38

Figure 3.8.	Circumferential Strains 20.75 Inches from the Closest End Plate, of Different Densities, to the Explosive Charge . . . . .	38
Figure 3.9.	Circumferential Strains 37.5 Inches from the Closest End Plate, of Different Stiffness, to the Explosive Charge . . . . .	39
Figure 3.10.	Longitudinal Strains 37.5 Inches from the Closest End Plate, of Different Stiffness, to the Explosive Charge . . .	40
Figure 3.11.	Nodal Velocities of Both End Plates of Stiffness Ten Times Lower Than the Nominal Value for 6061-T6 Aluminum . . .	41
Figure 3.12.	Measured and Computed Longitudinal Strains at 37.5 Inches from Closest End Plate to Explosive . . . . .	43
Figure 3.12.	(cont.) Measured and Computed Longitudinal Strains at 37.5 Inches from Closest End Plate to Explosive . .	44
Figure 3.13.	Measured and computed longitudinal strains at 38.5 inches from closest end plate to explosive . . . . .	46
Figure 3.14.	Measured and Computed Longitudinal Strains at 4.5 Inches from Closest End Plate to Explosive . . . . .	47
Figure 3.14.	(cont.) Measured and Computed Longitudinal Strains at 4.5 Inches from Closest End Plate to Explosive . . . . .	48
Figure 3.15.	Measured and Computed Longitudinal Strains at 3.5 Inches from Closest End Plate to Explosive . . . . .	49
Figure 3.16.	Measured and Computed Longitudinal Strains at 20.75 Inches from Closest End Plate to Explosive . . . . .	50
Figure 3.17.	Pressure Wave Propagation History in Near-Field Explosion Model . . . . .	52

Figure 3.18.	Cavitation at End Plate Closest to Near-Field Explosion . . . . .	53
Figure 3.19.	Near-Field Model Locations Chosen for Analysis . . . . .	55
Figure 3.20.	Local Deformations for Near-Field Models . . . . .	57
Figure 3.21.	Circumferential Strains at Both Sides of Stiffener Closest to Explosive Charge . . . . .	58
Figure 3.22.	Circumferential Strains at Both Sides of Stiffener Farthest from Explosive Charge . . . . .	59
Figure 3.23.	Circumferential Strains at Both Stiffeners of Two-Stiffener Model . . .	60
Figure 3.24.	Circumferential Strain Comparison for Unstiffened and One-Stiffener Models . .	62
Figure 3.25.	Longitudinal Strains (Unstiffened and Two-Stiffened) at Stiffener Location Closest to Charge . . . . .	63
Figure 3.26.	Longitudinal Strains (Unstiffened and Two-Stiffened) at Stiffener Location Far from Charge . . . . .	64
Figure A.1.	Load-Displacement Curve for 6061-T6 Aluminum . . . . .	69
Figure A.2.	Stress-Strain Curve for 6061-T6 Aluminum . . . . .	70

## **ACKNOWLEDGEMENTS**

I would like to express my gratitude to Professors Young W. Kwon and Young S. Shin for their guidance, encouragement and support in carrying out this research. In appreciation to Dr. Thomas T. Tsai and Dr. Kent Goering, from the Defense Nuclear Agency, for supporting this research. I would also like to thank LCDR Padraic Fox and LT James Chisum for their assistance in this research. Finally, I am most grateful to my mother Sylvia for her moral support and encouragement during my two years at the Naval Postgraduate School.

## I. INTRODUCTION

Because of the U.S. Navy's high interest in the underwater shock hardening effects on surface ships and submarines, this research intends to provide more insight into the response of a submerged vessel subjected to end-on underwater shock.

A continuous research has been taken at the Naval Postgraduate School to provide more insight into the deformation and catastrophic failure of surface and subsurface hulls. With simple cylindrical shells as a starting point, the study will then be extended to structures with more complex material and geometric properties as the methods and predictions improve.

Some of the previous studies in this subject are listed in references 1-3. These studies have served as building blocks for the current research into dynamic response of cylindrical shells to underwater shock. The objective of this study is to provide insight into the end-on shock dynamic response of cylindrical shells by using numerical and experimental techniques.

An unstiffened cylinder subjected to a far-field explosion was investigated using both numerical and experimental techniques. In addition, both unstiffened and ring-stiffened cylinders subjected to a near-field explosion were studied

numerically. Both the finite element and the boundary element methods were utilized for the numerical study.

## II. ANALYSIS AND EXPERIMENT

### A. NUMERICAL ANALYSIS

The numerical study of the behavior of cylindrical shells loaded by underwater explosion was carried out by using the finite element and boundary element methods.

For a problem with a three dimensional domain, the finite element method generates a three dimensional discretization of the entire domain whereas the boundary element method discretizes the surface boundary of the domain with a two dimensional grid. The boundary element method reduces significantly the number of elements required to model the problem by using a two dimensional mesh. Furthermore, the boundary element method surpasses the finite element method in computing tractions because these tractions are treated as primary but not secondary unknowns [Ref. 4]. The matrix generated by the boundary element method is generally fully populated while the matrix generated by the finite element method is usually narrowly banded.

To study the propagation of the explosive pressure wave through the acoustic medium and its subsequent interaction with the cylindrical shell, a finite element analysis program called VEC/DYNA3D [Ref. 5] was used. This program analyzes the deformations of solids which usually are inelastic in nature.

An alternative for modelling the acoustic medium is by using the boundary element method instead of using the finite element method. In doing so, the number of elements is greatly reduced. The boundary element analysis method program called USA (Underwater Shock Analyzer) [Ref. 6], was used to compute transient responses of submerged structures to acoustic shock waves.

In USA, the fluid-structure interaction was handled using the Doubly Asymptotic Approximation (DAA). The differential equation of motion describing the structure response is given below.

$$M_s \ddot{x} + C_s \dot{x} + K_s x = f \quad (1)$$

where  $M_s$ ,  $C_s$ , and  $K_s$  are the mass, damping and stiffness matrices respectively and  $x$ ,  $\dot{x}$ ,  $\ddot{x}$  are the displacement, velocity and acceleration vectors of the structure respectively. The excitation for a submerged structure subjected to an acoustic wave is given below.

$$f = -GA_f (P_i + P_s) + f_a \quad (2)$$

where  $-GA_f (P_i + P_s)$  is the force vector due to the fluid-structure interaction,  $f_a$  is the force vector applied to the dry structure,  $P_i$  is the incident pressure,  $P_s$  is the scattered pressure,  $G$  is the transformation matrix relating fluid and structure nodal forces and  $A_f$  is the diagonal area matrix associated with the fluid mesh.

To further study the fluid-structure interaction and especially to relate the scattered wave pressure to velocity over the wet surface, DAA was introduced. The DAA solution approaches the exact solutions for both early time and late time responses. The early time response is the high frequency response and the late time response is the low frequency response. The DAA is given by the following equation.

$$M_f \dot{P}_s + \rho c A_f P_s = \rho c M_f \dot{u}_s \quad (3)$$

where  $M_f$  is the symmetric fluid mass matrix for the wet-surface fluid mesh,  $u_s$  is the vector of scattered fluid particle velocities normal to the structure's wet surface,  $\rho$  is the density of the fluid,  $c$  is the sonic speed in the fluid and  $A_f$  is the symmetric fluid mass matrix for the wet surface fluid mesh. This matrix is created using the boundary element method.

The high frequency approximation, i.e. plane wave approximation implies that  $|\dot{P}_s| \gg |P_s|$  where  $\dot{P}_s$  is the time derivative of the acoustic pressure. Therefore, Equation (3) is converted into the following equation.

$$P_s = \rho c u_s \quad (4)$$

The low frequency approximation, i.e. virtual mass approximation implies that  $|\dot{P}_s| \ll |P_s|$ . The concept of virtual mass stems from the need to include a mass of fluid

surrounding that structure at the low frequency motion of the structure. Hence, Equation (3) is modified as seen below.

$$A_f P_s = M_f \dot{u}_s \quad (5)$$

Equation (3) denotes the first order of the Doubly Asymptotic Approximations (DAA1). The second order of the Doubly Asymptotic Approximations, DAA2, was created to improve the solution of DAA1 for intermediate times and to correct for curvature of the surface of the structure [Ref. 7].

The finite element model of both structure and fluid has the advantage of presenting the pressure wave propagation in the fluid and the fluid-structure interaction. On the other hand, it also requires a large number of elements. Using the finite element model for the structure and the boundary element model for the fluid reduces the number of degrees of freedom in the system because the fluid domain is usually much larger than the structural dimension. However, it cannot present the propagation of the pressure wave across the fluid.

The post-processing of the VEC/DYNA3D and USA programs was done using LS-TAURUS [Ref. 8]. This post-processor generates pressure, strain and stress contours superposed on the mesh or also generates element and node time history responses.

## **B. NUMERICAL MODELLING**

To study the deformation of a cylindrical shell subjected to an end-on shock, two numerical models were created. The

first model was designed to study the propagation of the pressure wave from the explosive to the cylinder and its early interaction with the cylindrical shell. The second model was designed to study stresses and strains of the cylindrical shell without analyzing the fluid or explosive around it.

To generate the first model, the pre-processor, INGRID [Ref. 9], generated the finite element meshes for the explosive, fluid and cylindrical shell and VEC/DYNA3D computed their dynamic response.

The computational effort was minimized by creating a quarter model, possible only because of the symmetric geometry of the charge and cylindrical shell locations. Appropriate symmetric boundary conditions were applied to the problem.

The explosive was modeled with a fine mesh of 416 elements to avoid non-spherical propagation and severe distortion in the finite element mesh as a result of the expansion of the explosive in the fluid.

To model the explosion, the Jones-Wilkins-Lee (JWL) equation of state was invoked to describe the pressure-volume-energy behavior of high explosives. [Ref. 10]

$$P = A \left( 1 - \frac{W}{R_1 V} \right) e^{-R_1 V} + B \left( 1 - \frac{W}{R_2 V} \right) e^{-R_2 V} + \frac{WE}{V} \quad (6)$$

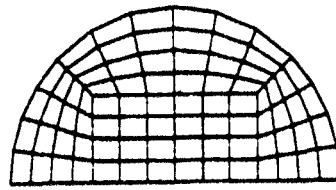
where A, B, and C are linear coefficients given in units of Mbar. R1, R2 and w are nonlinear coefficients, V is the volume of detonation products divided by the volume of undetonated

high explosive,  $P$  is the pressure, and  $E$  is the detonation energy per unit volume in  $(\text{Mbar cm}^3)/\text{cm}^3$ .

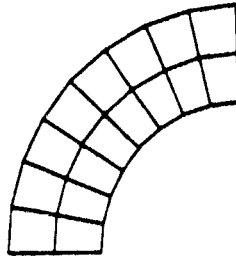
The Gruneisen equation of state was used to define the pressure for compressed materials, in this case water. This equation of state is provided in [Ref. 10].

The model including the charge, water and cylinder had 11808 elements which consequently required large amounts of storage. Finite element meshes are given in Figure 2.1. Therefore, the charge was constrained to be close to the target cylinder to minimize the elements between explosive and cylinder and still be able to store the shock wave propagation and stress wave effect information. The cylindrical shell of this finite element model was modified to add ring stiffeners. One model had one ring stiffener located halfway between the cylinder end plates. The second model had two ring stiffeners equidistant between the two end plates. A view of these two models is shown in Figure 2.2. The additional stiffeners only added an additional 16 elements per stiffener to the total. The ring stiffeners were added to study their effect in stress wave propagation and reinforcement properties.

The other model used in this research was designed to study the stresses and strains of the cylinder for comparison with experimental results of an actual underwater shock test. The model dynamic response was analyzed using both VEC/DYNA3D and USA. The finite element method was used for the cylindrical shell and the boundary element method was used for



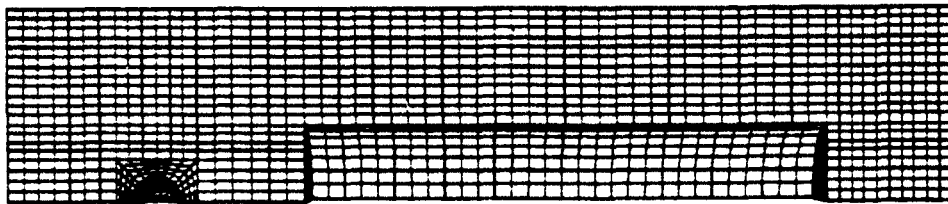
(a) Quarter Sphere



(b) Quarter Stiffener

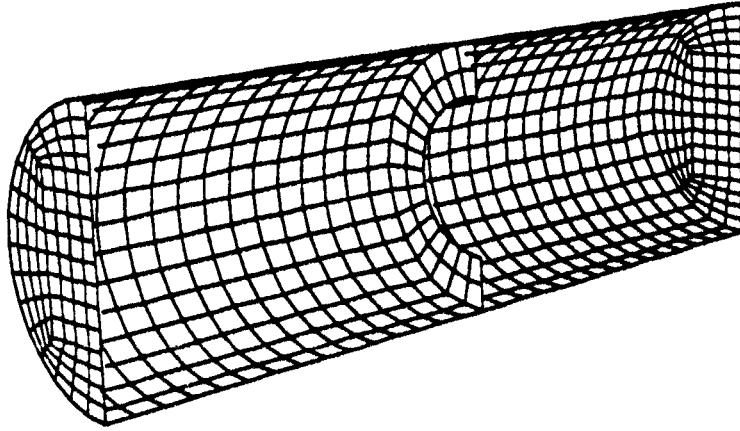


(c) Quarter Cylindrical Shell with End Plates

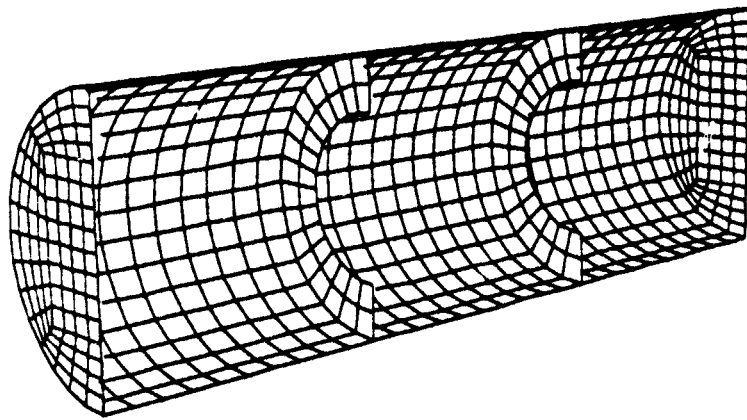


(d) Quarter Fluid Mesh

**Figure 2.1. Finite Element Meshes for Near-Field Explosion**



(a) One-Stiffener Model

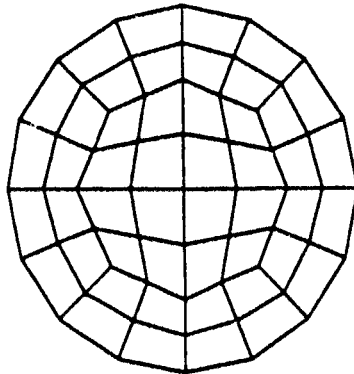


(b) Two-Stiffener Model

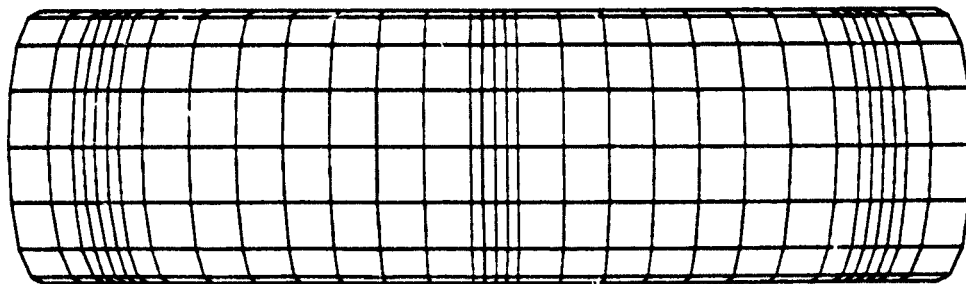
**Figure 2.2. Stiffened Cylinders with End Plates**

the fluid-structure interaction. This model consisted of a cylindrical shell capped at both ends by two end plates. The cylindrical shell had 512 elements and the endplates had 48 elements each. The full model had 608 total elements. A diagram of this model is presented in Figure 2.3. The different size of the cylindrical shell elements was generated to get a better solution in the strain gage locations of the experiment. These locations will be presented when the experimental procedure is explained.

A study of grid independence and time step instability was performed to verify that the choice of the element sizes and time steps chosen were not affecting the solution. To analyze grid independence, three different discretizations were made over a four inch segment of the cylinder. The discretization was made in the longitudinal direction due to the symmetry of the problem. The coarse model had two elements of two inches each in the axial direction. The finer model had six elements of 0.66 inches each in the same direction. The finest mesh model had eighteen elements of 0.22 inches each. The three discretizations are shown in Figure 2.4. Comparison of the three models revealed considerable differences between the coarse model and the two finer mesh models. The six and 18 element models had almost identical results. As a result of this comparison, the six element model was chosen as a good estimate of the size of the elements to use for the actual model.

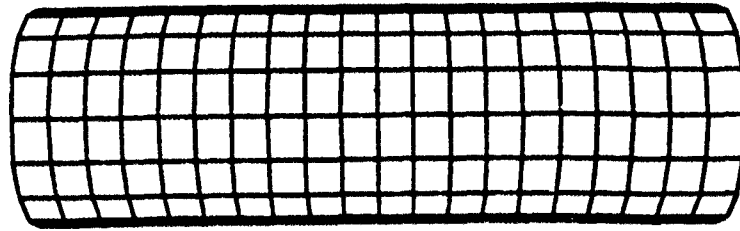


(a) End plate

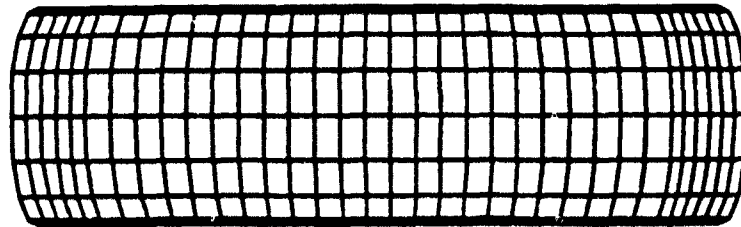


(b) Cylindrical shell

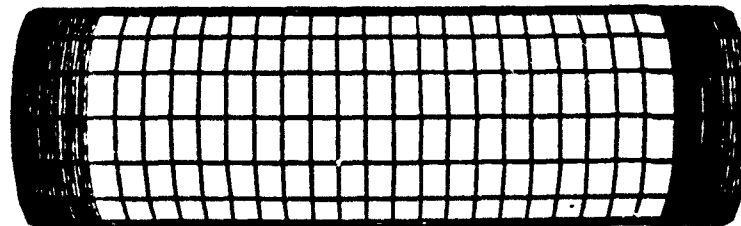
**Figure 2.3. Finite element meshes of a cylinder subject to a far-field explosion**



(a) Coarse model (2 inch elements)  
(2 elements in 4 inch span)



(b) Finer model (0.66 inch elements)  
(6 elements in 4 inch span)



(c) Finest model (0.22 inch elements)  
(18 elements in 4 inch span)

**Figure 2.4. Finite element discretization over 4 inch span at one end of cylinder**

Another area of concern was the effect the time step would have on the solution. An appropriate method to choose a stable time step size was the Courant-Friederichs-Lewy Criterion. The equation for this criterion is given below.

$$\Delta t \leq l / c \quad (7)$$

where  $\Delta t$  is the time step size,  $l$  is the length of the element, and  $c$  is the sonic speed in 6061-T6 Aluminum.

Two different time step sizes were chosen,  $2 \times 10^{-6}$  and  $2 \times 10^{-7}$  seconds. These time steps satisfied the above mentioned criterion. The resulting solutions for the two time steps were almost identical. Therefore,  $4 \times 10^{-7}$  seconds was chosen as the time step for this problem since this value was between the two chosen for the criterion verification.

### **C. UNDERWATER EXPLOSION TEST**

The underwater explosion test was performed at Dynamic Testing Inc. (DTI) facilities in Rustburg, Virginia. This facility had a quarry that had been filled with water for use in underwater shock tests. The water depth was approximately 130 feet at the location of the test which was deep enough to allow the study of the dynamic response of the cylinder prior to the arrival of the reflected shock wave from the bottom.

The cylinder was placed 12 feet below the water's surface and held in place by a crane with pendants attached to both front and rear end plates. The rig attachment can be observed

in Figure 2.5. The 60 pound charge of HBX1 was also placed 12 feet below the surface and aligned with the cylinder with a span wire from the charge float to the crane rig. Figure 2.6. gives a good view of the arrangement. The 12 foot depth was chosen so that the bubble generated by the explosion would vent to the surface prior to encountering the cylinder. The test geometry is shown in Figure 2.7. The explosive charge was activated by a radio device and the plume is pictured in Figure 2.8.

The strain gages used for this test were of type CEA-06-250UW-350. These are general purpose strain gages with an optimum operating range of  $\pm 1500$  micro strain and are used for both static and dynamic test measurements. They were attached to the cylinder using a M bond 200. There were a total of seven strain gages placed at locations A, B and C, as seen in Figure 2.9, per axis for a total of 14 strain gages. The cylinder was oriented so that the gages at C would be closest to the explosive charge. A pressure probe was also placed 28 feet from the cylinder to measure the free field pressure.

The cylinder used for the underwater shock test was manufactured from 6061-T6 Aluminum. This alloy is primarily an Aluminum-Magnesium-Silicon alloy. The T6 denomination indicates it was solution treated and artificially aged [Ref. 11]. The cylinder consisted of a quarter inch thick cylindrical shell and two one-inch thick circular end plates



Figure 2.5. Cylinder and Crane Rigging

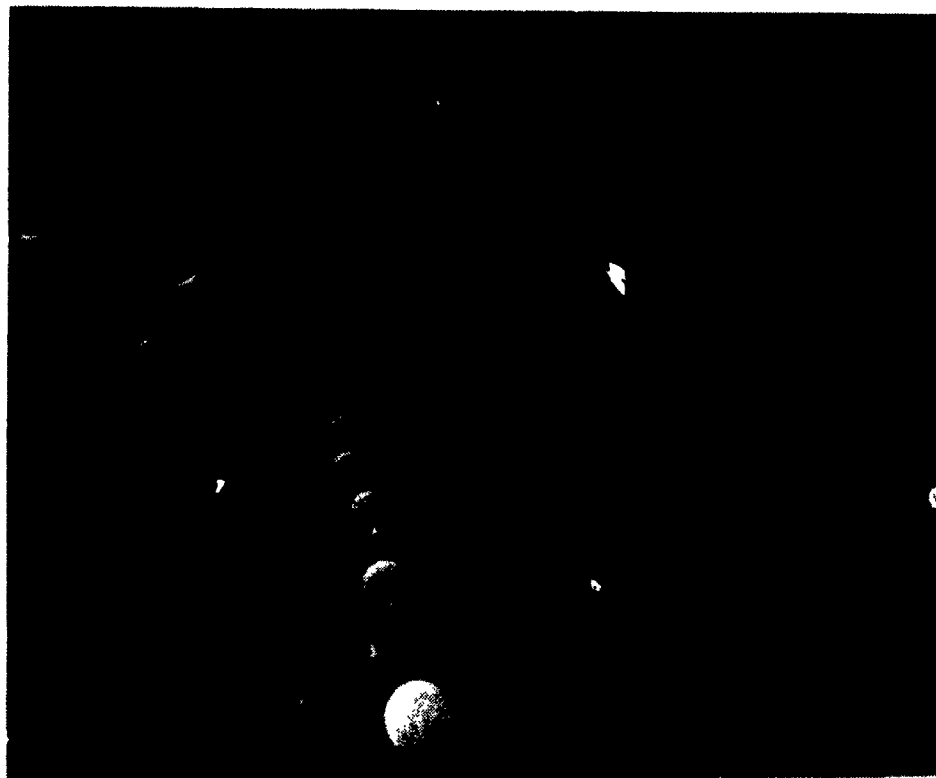


Figure 2.6. Test Geometry at the Surface

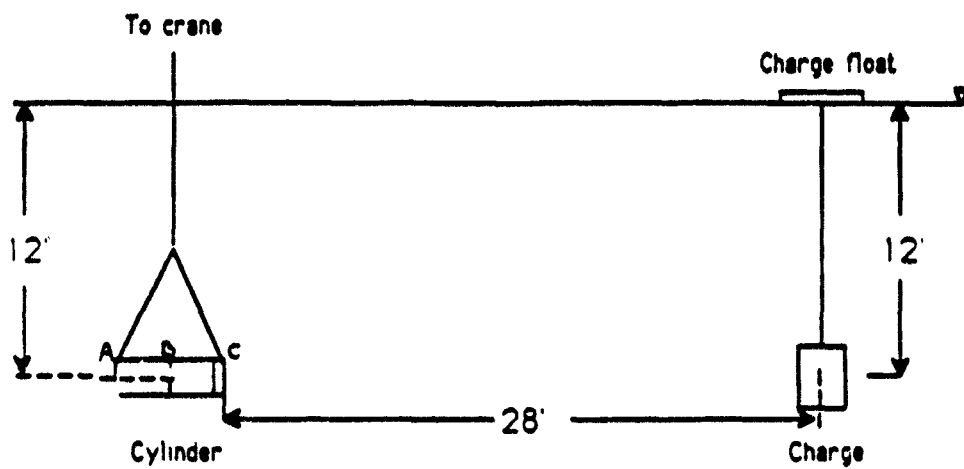


Figure 2.7. Test Geometry (Ranges in Feet)



Figure 2.8. Water Plume from Shot

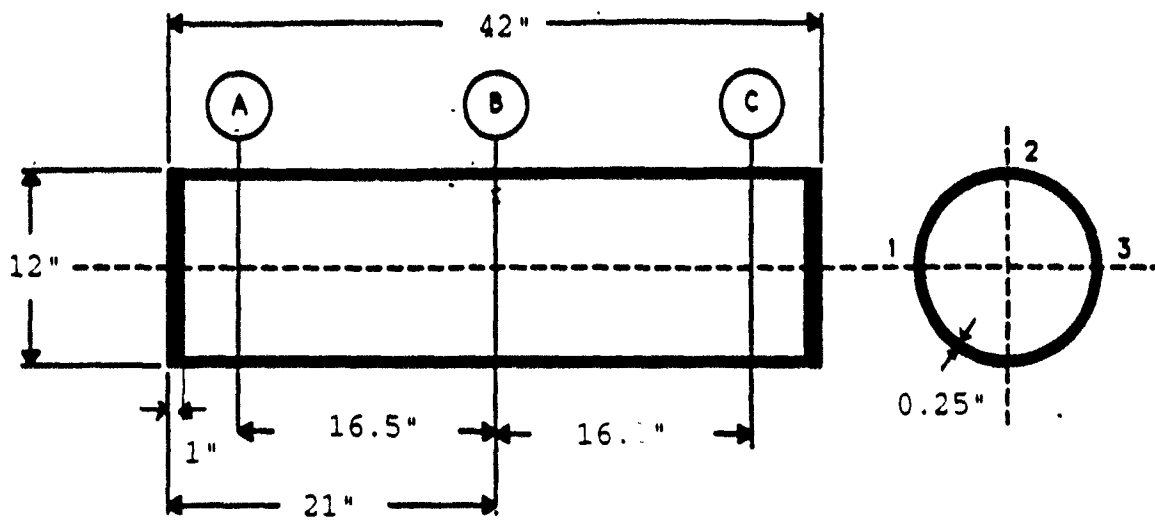


Figure 2.9. Cylinder Geometry

as seen in Figure 2.9. The welding of the two end plates to the cylindrical shell was done at the Naval Postgraduate School facilities. There was a concern in the welding process of the two circular end plates to the shell because of the heat generated at the weld and its effect on the alloy morphology close to the weld. However, the strain readings were taken far enough from the heat affected zone to have any measurable effect on the readings. The welding was done using tungsten inert gas (TIG). This procedure has been recommended by most expert welders [Ref. 12].

The cylinder weighed 60.5 pounds and tensile tests were done to verify that the material properties were close to the nominal properties of 6061-T6 Aluminum. This test can be seen in the Appendix. The value of Young's Modulus was 10800 ksi and the yield strength was approximately 43 ksi.

Post-shot observation showed no visible deformations on the cylinder as seen in Figure 2.10. All strain gages were well fixed when uncovering the bonding material. Only strain gage C1 in Figure 2.9. was found wet when uncovered suggesting the possibility of water insertion.



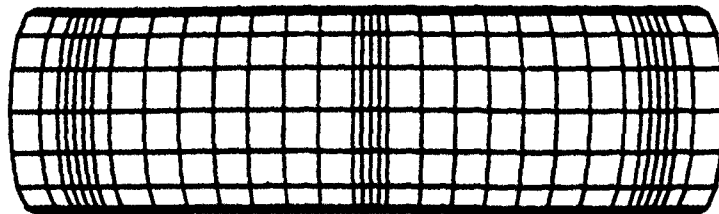
**Figure 2.10. Post-Shot View of Cylinder**

### III. RESULTS AND DISCUSSIONS

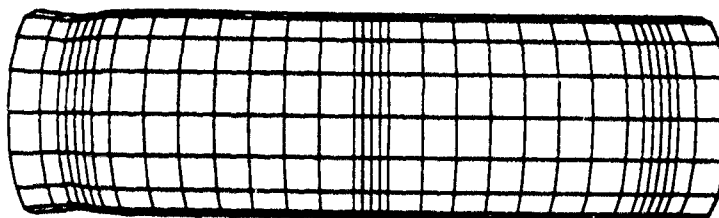
#### A. NUMERICAL RESULTS OF FAR-FIELD EXPLOSION

A cylinder was subjected to an end-on explosion with a standoff distance. The sketch of the configuration was presented in previous Figure 2.6. The deformations of the cylinder are shown in Figure 3.1 at different times as the shock wave propagates along the axial direction of the cylinder. Because of the symmetric loading, the deformation was axially symmetric. In order to visualize the deformations more clearly, the actual deformations were magnified by the scale factor shown in Figure 3.1.

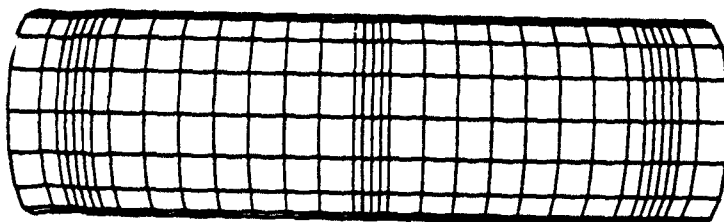
As the shock pressure wave hit one end plate, which is at the nearest location from the charge, the compressive stress wave propagated from the end plate to the other end plate through the aluminum alloy cylinder with a faster speed of sound than the shock pressure wave propagating through the surrounding water medium. The nearer end plate will be called the near plate while the other end plate will be called the remote end plate in the following discussion. The shock load caused initially a localized circumferential deformation close to the near end plate as shown in Figure 3.1c. This localized deformation remained as a permanent deformation. As the shock pressure wave propagated toward the remote end plate, it



(a) time = .00000E00 sec

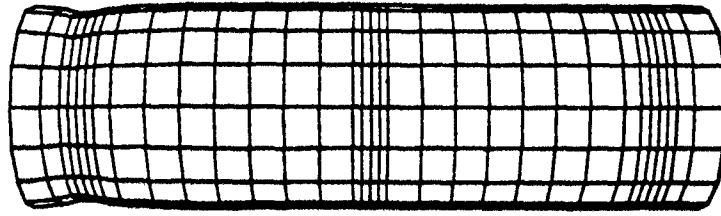


(b) time = .79600E-04 sec

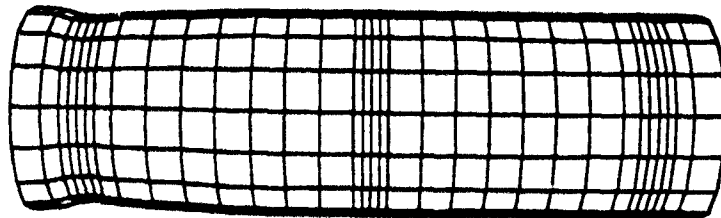


(c) time = .11960E-03 sec  
disp. scale factor = 1.00E+01

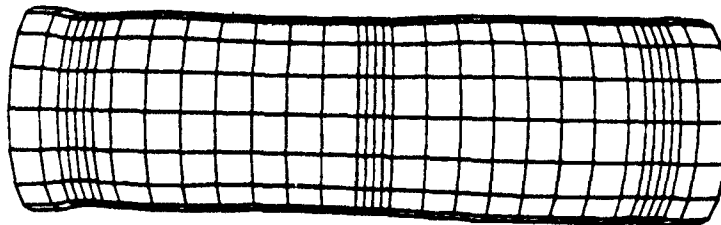
**Figure 3.1. Deformation Time Histories**



(d) time = .15960E-03 sec



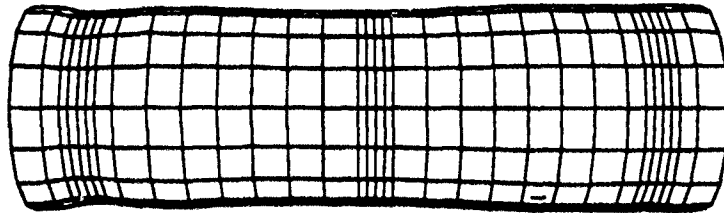
(e) time = .23960E-03 sec



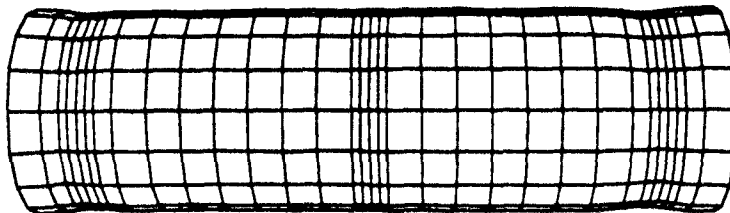
(f) time = .47960E-03 sec

disp. scale factor = 1.000E+01

**Figure 3.1. (cont). Deformation Time Histories**



(g) time = .51960E-03 sec



(h) time = .11596E-02 sec  
disp. scale factor = 1.000E+1

**Figure 3.1 (cont.) Deformation Time Histories**

induced a radial contraction of the cylinder wall and subsequently a recovery of it. After the shock pressure wave passed the remote end plate, there was also a localized circumferential deformation near the remote end plate as shown in Figure 3.1h. The overall steady state deformation of the cylinder was nearly symmetric about the center plane which is located at an equal distance between the two end plates. At this stage, the cylinder had the deformation near the two end plates, and the rest of the cylinder had very little radial deformation. The axial deformation of the cylinder had an accordion mode as expected. Figure 3.2 is the plot of axial velocities at the centers of the two end plates. The two velocities had a phase difference of 180 degrees. The phase difference indicated the accordion mode.

The initial localized circumferential deformation near the end plates may be explained as follows. The axisymmetric deformation of a shell has the following governing equation.

$$D \frac{d^4 w}{dx^4} + F \frac{d^2 w}{dx^2} + Eh \frac{w}{a^2} = P \quad (8)$$

where  $w$  is the radial deflection,  $x$  is the axial direction,  $D$  is the flexural rigidity of the shell,  $E$  is the elastic modulus,  $h$  is the wall thickness of the shell,  $a$  is the shell radius, and  $F$  and  $p$  are the axial load and the radial load, respectively. Therefore, the effect of the inertia term on the deformation was negligible. The axial load applied on the cylinder due to the shock pressure was lower than the critical

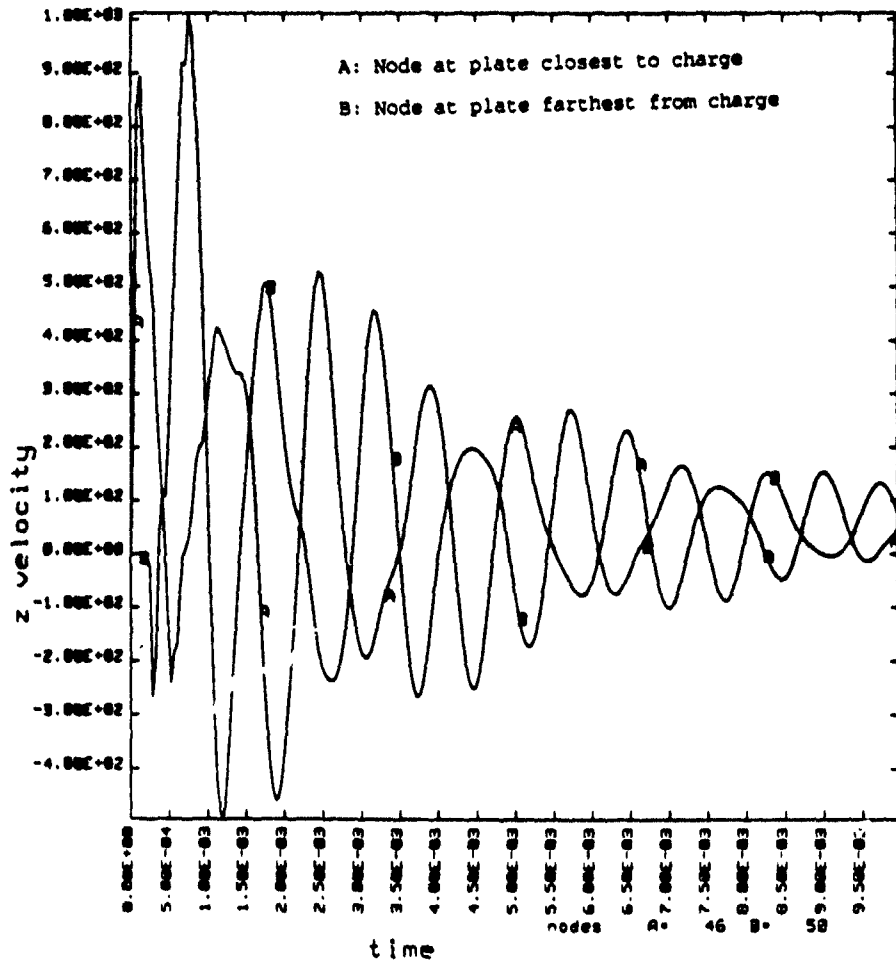
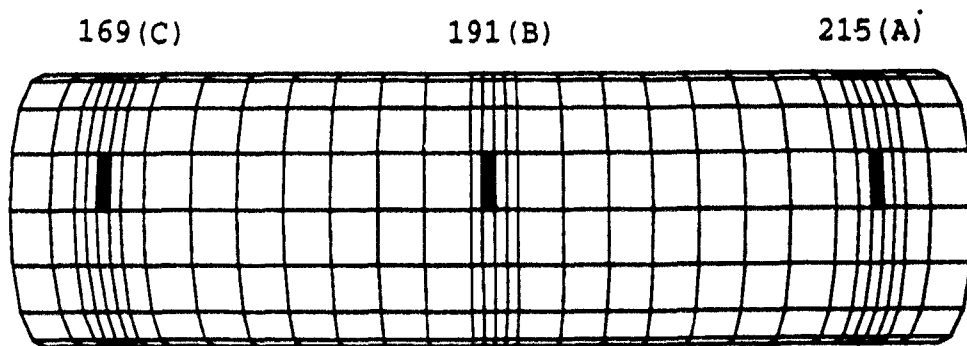


Figure 3.2. Axial Velocities of Nodes at Both End Plates of Cylinder

buckling load of that cylinder from the linear buckling theory. In this case, the deformation of the cylinder was of a decaying exponential form and it damped out rapidly if the cylinder was not short [Ref. 13]. The very stiff end plates suppressed the deformation very near the end plates. This resulted in a shift of the locations of the circumferential deformation somewhat away from the end plates. The inertial force was not included in the equation. When the density of the cylinder was varied from its nominal value to a value of one order of less magnitude, the same kind of initial localized deformation was observed. However, the low density caused less permanent localized deformation.

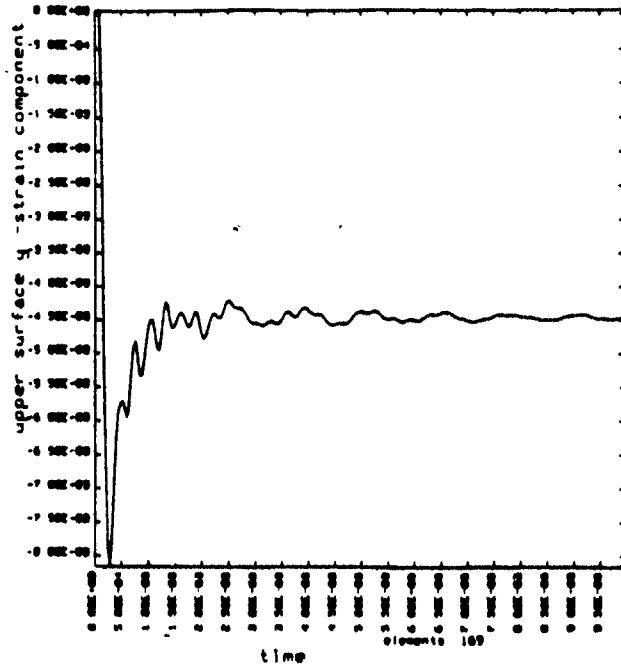
Two normal strain components, i.e., hoop (or circumferential) and axial (or longitudinal) strains, were computed at some selected locations. The selected points were located at the locally deformed zones as well as at the center of the cylinder. The locations where the strains were computed are illustrated in Figure 3.3. Strain gages were also attached to the same locations on the cylinder in the experimental study for the comparison with the numerical study. All the strains were computed and measured at the outside surface of the cylinder. The comparison between the numerical and experimental results will be provided in the next section. As shown in the strain plots of Figure 3.4, the circumferential strains at locations A and C of Figure 3.3 were very close to each other. The strains had initially large compressive peaks



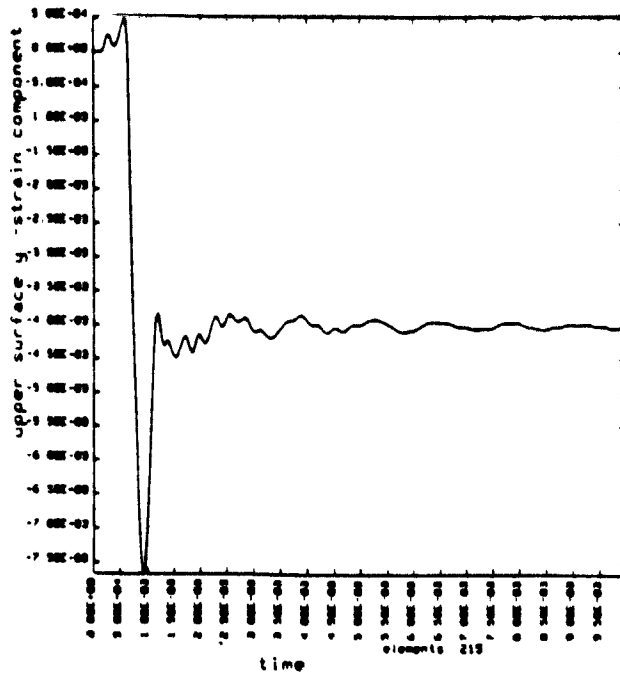
Explosion  
side

1. Element 169: 4.5" from closest end to explosion.
2. Element 191: 20.75" from closest end to explosion.
3. Element 215: 37.5" from closest end to explosion.

**Figure 3.3 Locations for Strain Computation**



(a) Circumferential Strain 4.5 in. from End Plate Closest to Explosive Charge



(b) Circumferential Strain 37.5 in. from End Plate Closest to Explosive Charge

**Figure 3.4** Circumferential Strains Close to End Plates

and returned to the steady state values which were about half the initial peak strain values. Location A had a small circumferential tensile strain before arrival of the shock pressure wave. The small tensile strain was caused by the longitudinal compressive stress wave which arrived at the location through the cylinder. The longitudinal compressive strain caused by the longitudinal stress wave resulted in the circumferential tensile strain because of Poisson's effect. After the shock pressure wave arrived at the location, the circumferential strain became compressive. The circumferential strain at the middle of the cylinder, i.e, location B in Figure 3.3, was much less than those at locations A and C as shown in Figure 3.5 because the localized deformations at locations A and C induced the larger circumferential strains.

The initial peak of longitudinal strain was compressive at all locations due to the propagation of the longitudinal compressive stress wave after the shock pressure hit the near end plate. The early arrival of the shock pressure wave to location C in Figure 3.3, caused the immediate jump of the longitudinal strain into tension after the initial compression. On the other hand, the subsequent compressive stress wave resulted in more compression at locations A and B than at location C until the shock pressure wave arrived at the locations. At later times the longitudinal strain were quite different at locations A and C. The longitudinal strain at location A stayed in tension just after the initial

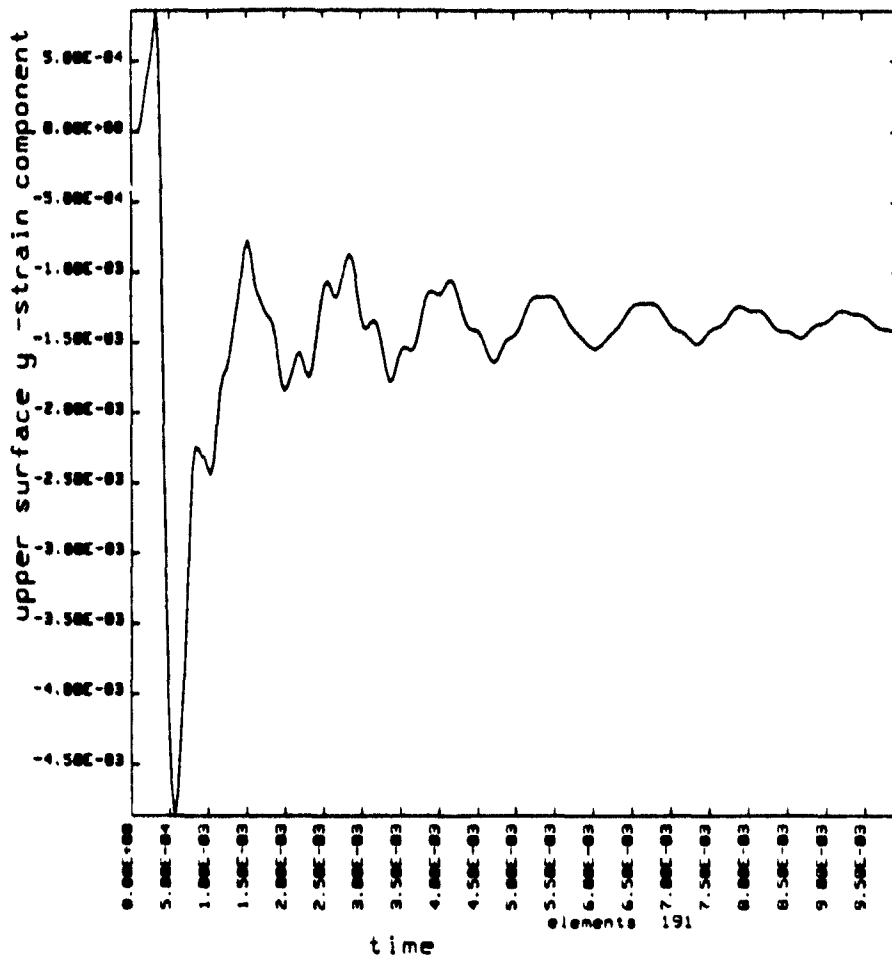
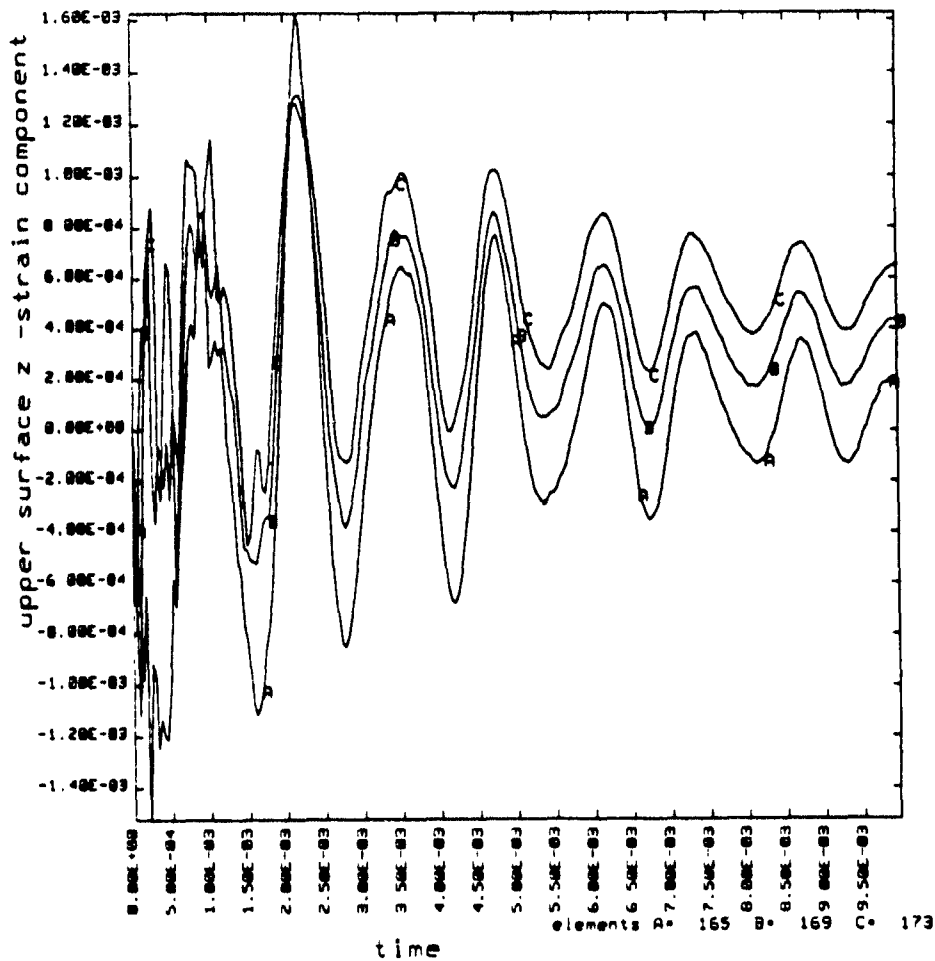


Figure 3.5. Circumferential Strain 20.75 Inches from the Closest End Plate to the Explosive Charge

compressive peak while the longitudinal strain at location C alternated between tension and compression. However, the longitudinal strain was quite sensitive with the locations near A and C because of the localized deformation. Longitudinal strains at various locations near position C were plotted in Figure 3.6. The approximate frequency of the longitudinal strains after the initial compression was about 750 Hz at all locations.

The present study showed that the end plates played an important role in the deformation of the cylinder. Some parametric study was performed to find the effect of the end plates on the dynamic response of the cylindrical shell. The first study was to find out the effect of the inertial force of the end plates. Therefore, the density of the end plates was reduced tenfold with the stiffness of the plates remaining the same. The light end plates had a larger effect on the longitudinal strains than on the circumferential strains. The frequency of the longitudinal strains was approximately 840 Hz for the light end plates. This frequency was higher than that for the heavy plates as expected. The longitudinal strain damped more quickly with the light end plates than with heavy end plates as shown in Figure 3.7. The light end plates resulted in an approximately 30% decrease of the circumferential strain at location C while its effect was negligible on the circumferential strain at location A. Moreover, the circumferential strain at location B increased



- A. (165) 4.0 inches from end plate
- B. (169) 4.5 inches from end plate
- C. (173) 5.0 inches from end plate

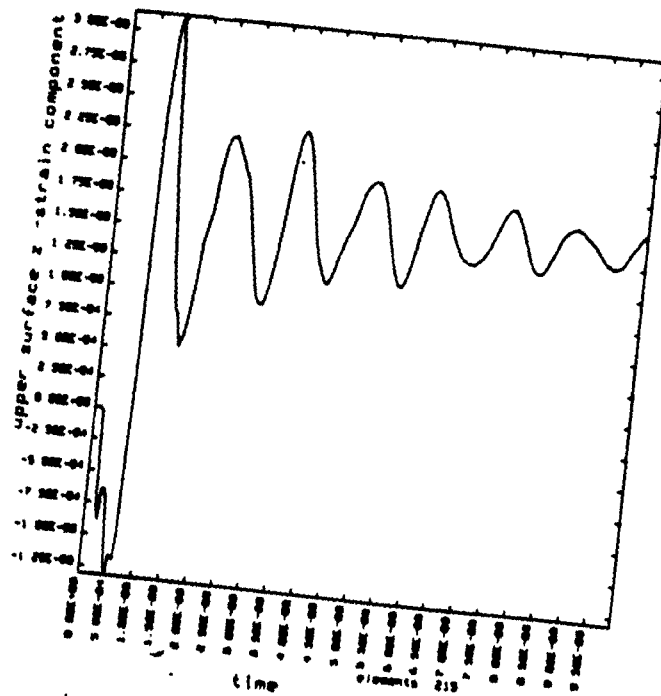
**Figure 3.6. Longitudinal Strains in the Vicinity of the Closest End Plate to the Explosive Charge**

about 20 percent for the light end plates as shown in Figure 3.8.

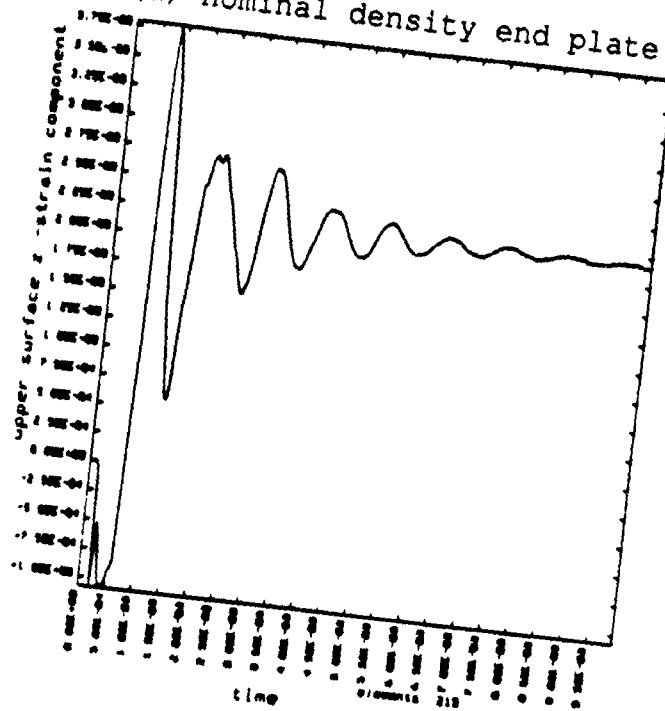
The next parametric study was performed to investigate the effect of stiffness of the end plates on the deformation of the cylinder. The elastic modulus of the plate was reduced tenfold without change of the rest of the material data. The less stiff end plates made an effect on not only longitudinal strain but also circumferential strain as shown in Figures 3.9 and 3.10. The less stiff support of the cylinder at the end plates caused more fluctuation in the circumferential strain as shown in Figure 3.9. The wave pattern in the longitudinal strain-time history plot was also severely altered by the less stiff end plates as shown in Figure 3.10. The longitudinal velocities of the centers of the less stiff end plates were plotted in Figure 3.11 and showed a very different pattern than the accordion oscillation of the stiff plates in Figure 3.2. The density change in the previous parametric study did not show a different velocity pattern of the end plates.

## **B. COMPARISON BETWEEN NUMERICAL AND EXPERIMENTAL RESULTS**

An underwater explosion test was performed at Dynamic Testing Inc. facilities in Rustburg, Virginia as described in Chapter II. Unfortunately, a pressure gage, placed to measure a free-field pressure at the same stand-off distance as the cylinder, failed. Therefore, no information was available for the shock pressure due to the charge. The previous numerical

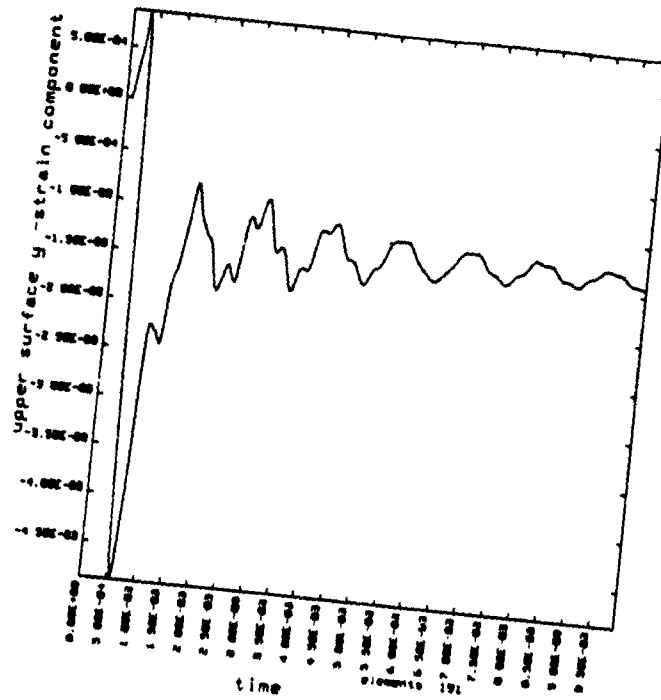


(a) nominal density end plate

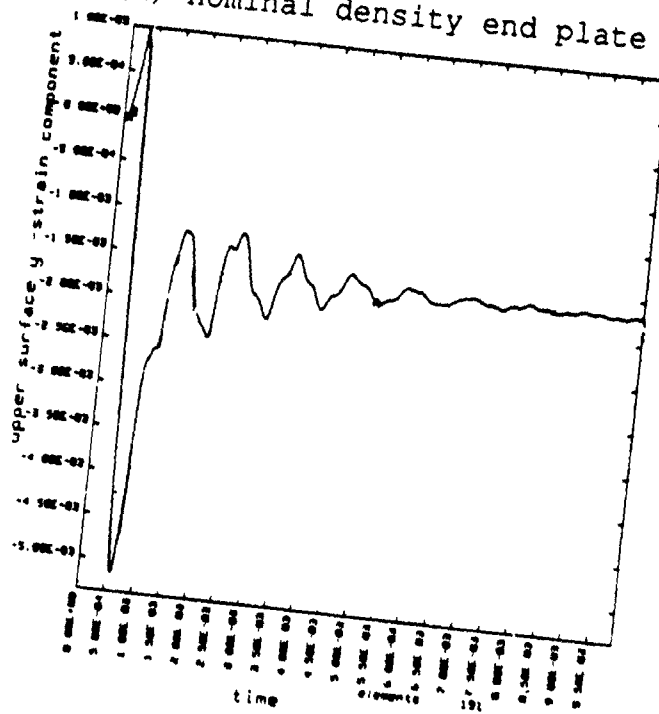


(b) lower density end plate (order of ten)

Figure 3.7. Longitudinal Strains 37.5 Inches from the Closest End Plate, of Different Densities, to the Explosive Charge

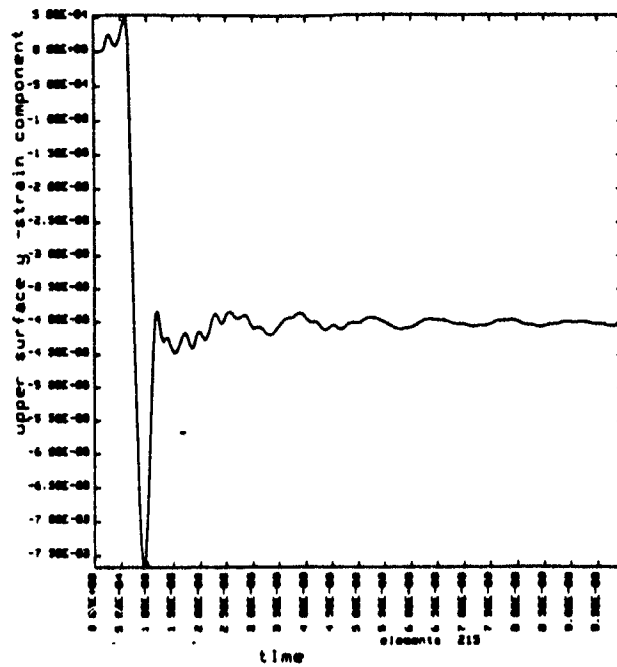


(a) nominal density end plate

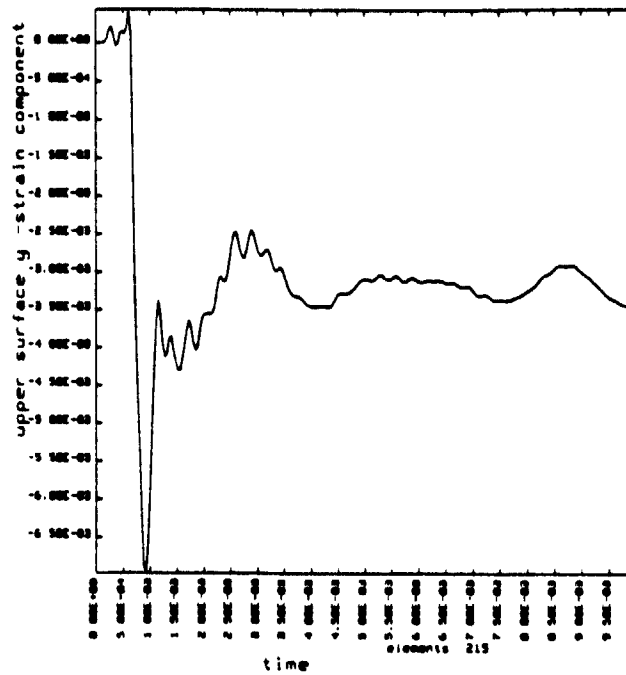


(b) lower density end plate (order of ten)

**Figure 3.8. Circumferential Strains 20.75 Inches from the Closest End Plate, of Different Densities, to the Explosive Charge**

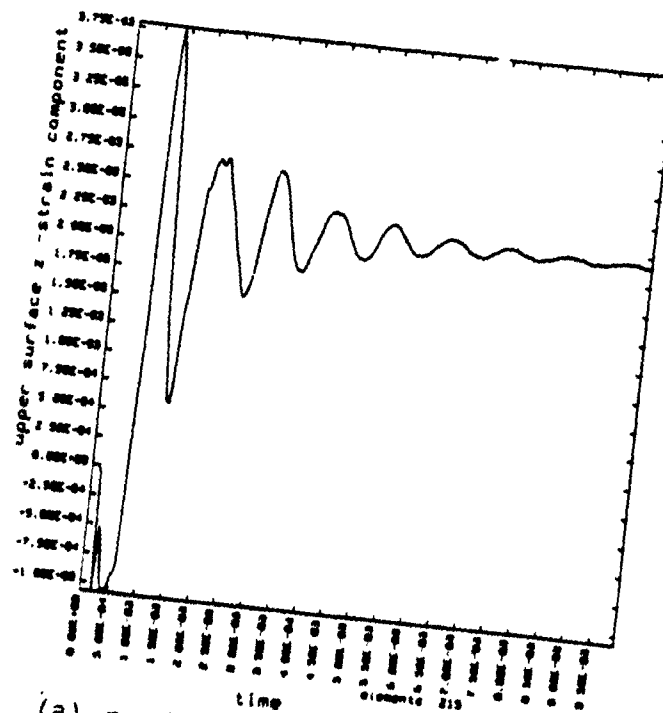


(a) nominal stiffness end plate

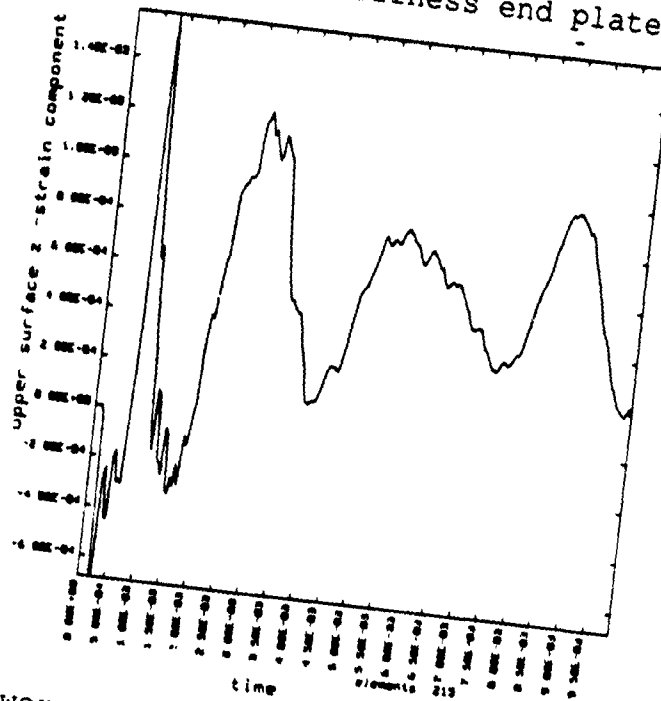


(b) lower stiffness end plate (order of ten)

**Figure 3.9. Circumferential Strains 37.5 Inches from the Closest End Plate, of Different Stiffness, to the Explosive Charge**



(a) nominal stiffness end plate



(b) lower stiffness end plate (order of ten)

Figure 3.10.

Longitudinal Strains 37.5 Inches from the  
Closest End Plate, of Different Stiffness, to  
the Explosive Charge

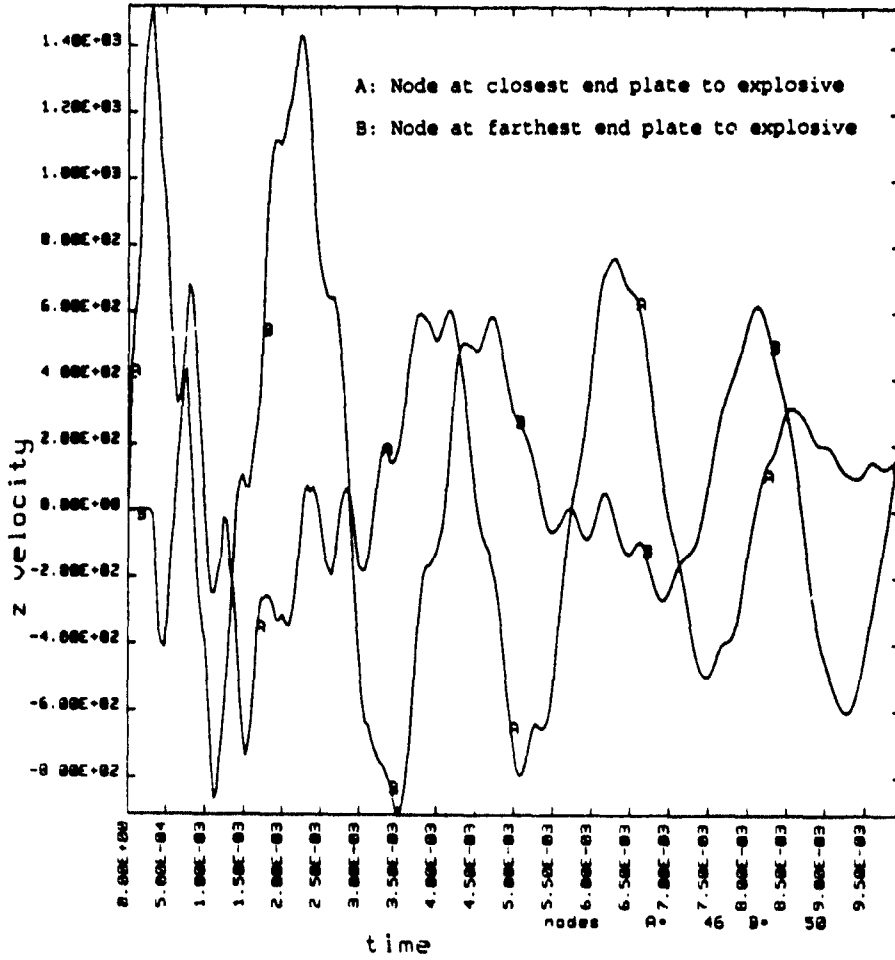
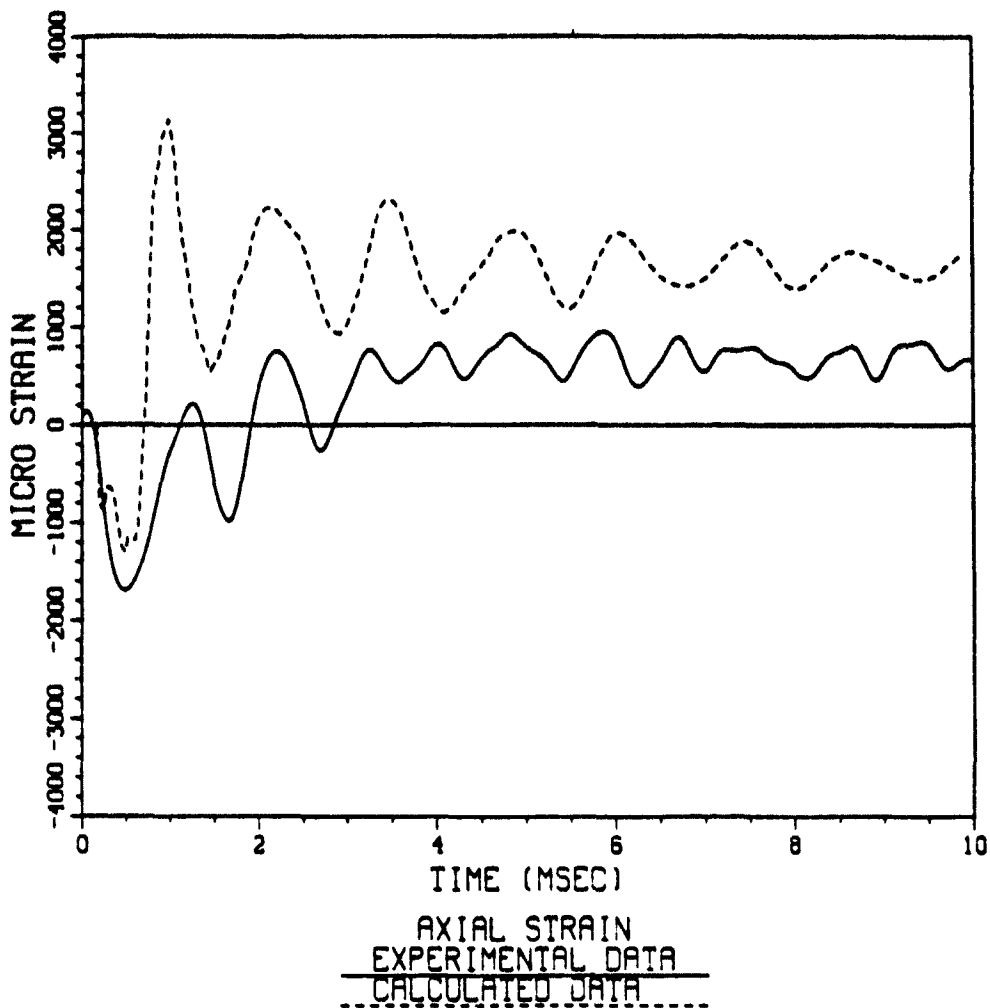


Figure 3.11. Nodal Velocities of Both End Plates of Stiffness Ten Times Lower Than the Nominal Value for 6061-T6 Aluminum

simulation was carried out using the empirical equation for pressure with the nominal weight of the charge. As a result, the following comparison was made in a qualitative sense. In addition, several strain gages failed before and during the test. All the strain gages to measure circumferential strains failed. Only the axial strains were compared here.

The speed of sound in the water was computed based on the arrival time of the pressure wave to the strain gage from the explosion and the stand-off distance. The computed speed of sound was close to a nominal value of 5000 ft/sec. Then locations of the strain gages were shown in Figure 3.3. The longitudinal strain at gage location A was compared in Figure 3.12. All experimental data was filtered out at 2000 Hz low pass. Therefore, there was no peak strain with a higher frequency than 2000 Hz in the experimental data. Both numerical and experimental solutions indicated the initial compression and tension at later times. They agreed well qualitatively even if there was a mismatch in magnitude. The longitudinal strain was quite sensitive to the location. The longitudinal strain computed at just one inch away from the gage location was compared with the experimental measurement in Figure 3.13. Two strain gages, both of which were located at location A but were separated in the circumferential direction with an angle of 180 degrees, gave a similar longitudinal measurement as shown in Figure 3.12. This measurement indicated the axisymmetric nature of the

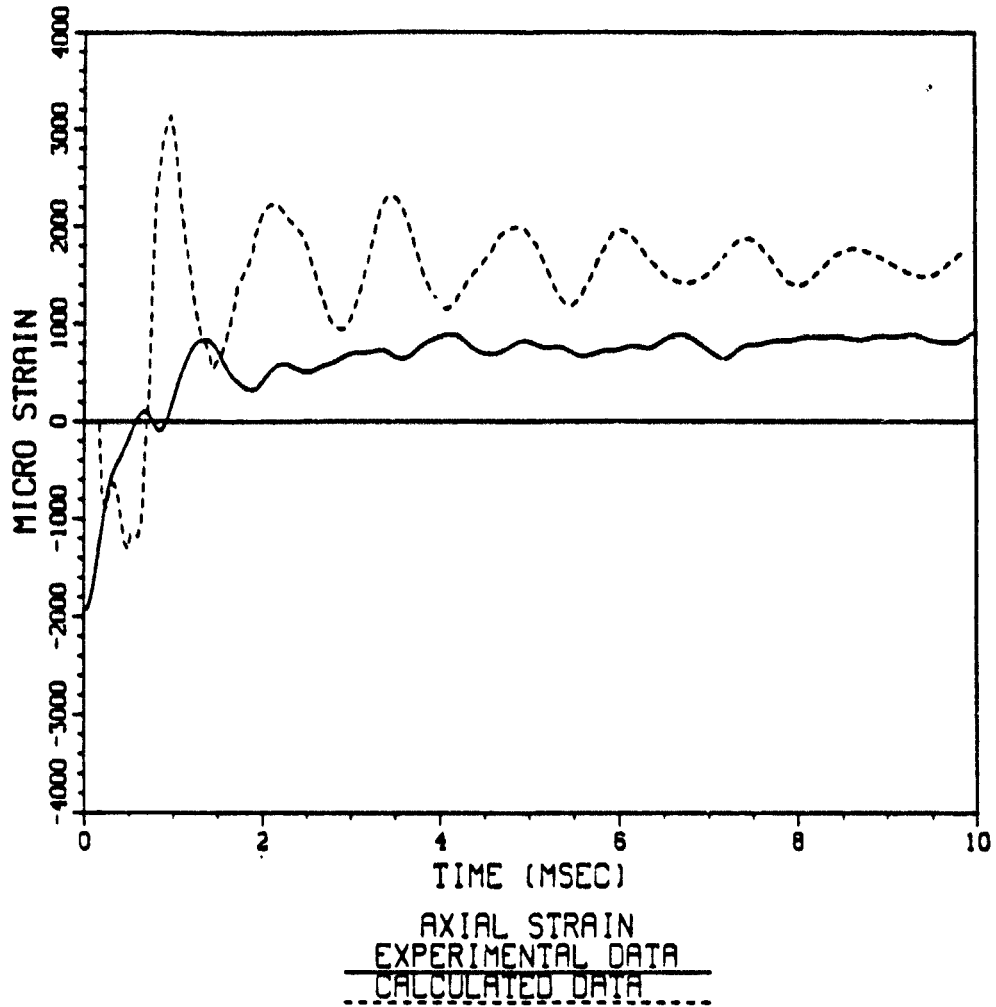
TEST 1, LOCATION A1L



(a) A1L Strain Gage Location (See Figure 2.9)

**Figure 3.12. Measured and Computed Longitudinal Strains at 37.5 Inches from Closest End Plate to Explosive**

TEST 1, LOCATION A3L



(b) A3L Strain Gage Location (See Figure 2.9)

Figure 3.12. (cont.) Measured and Computed Longitudinal Strains at 37.5 Inches from Closest End Plate to Explosive

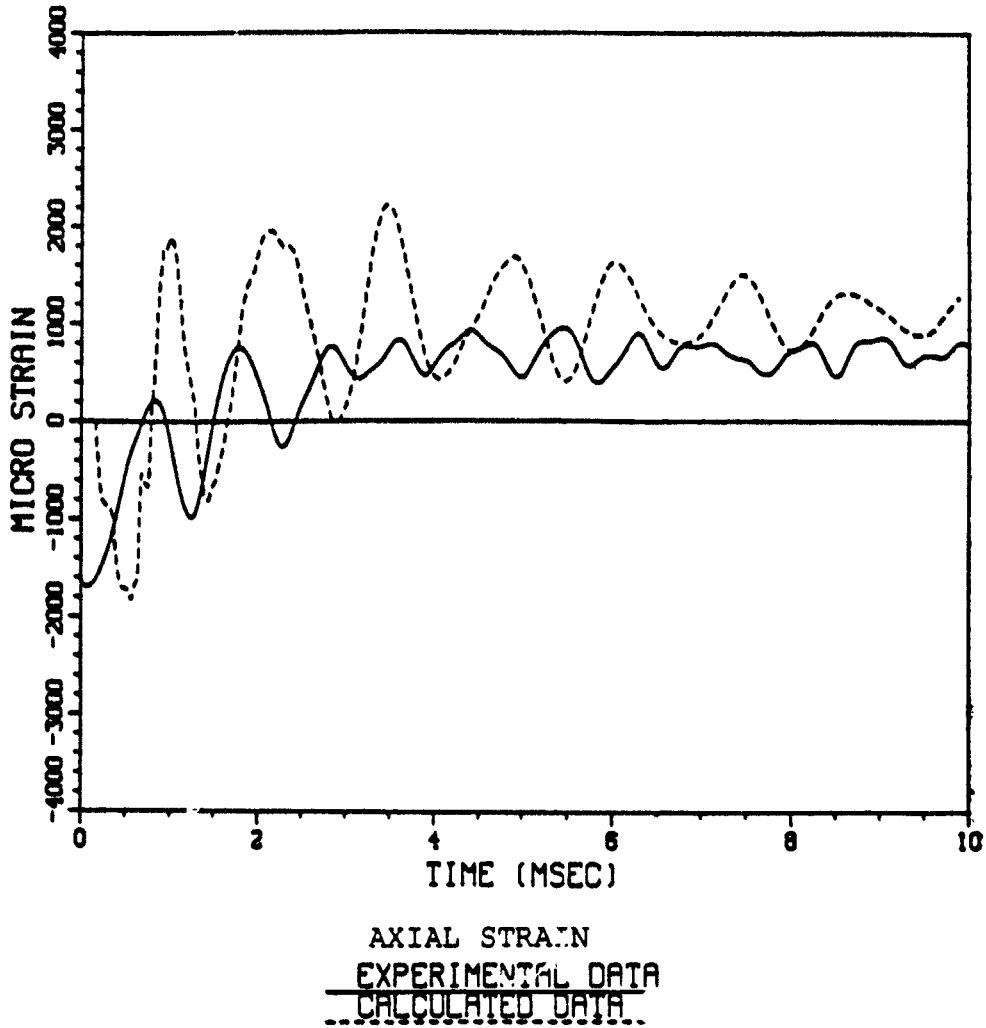
deformation. However, the two strain gages, which were placed at location C and were separated 180 degrees in the circumference, provided quite different longitudinal strains. This discrepancy in readings could have been caused due to observed water insertion in the strain gage at location C1.

Accordingly, the numerical result was not in good agreement with the experimental data as shown in Figure 3.14. The sensitivity of the location where the strains were computed was also evident for location C as shown in Figure 3.15. The experiment showed a compressed longitudinal strain while the numerical solution showed an oscillation of the strain from compression to tension. A small distance away from location C gave a different solution. However, the experimental data was still different from the numerical result. The longitudinal strain at gage location B was compared in Figure 3.16. The result was similar to that at gage location C. It was not clear at this time what the major cause of the discrepancy was. However, this was the first test of a series of underwater experiments to be performed. The discrepancy will be investigated from the following experiments with more available experimental data and numerical simulations.

### **C. NUMERICAL RESULTS OF NEAR-FIELD EXPLOSION**

The study of the dynamic response of cylindrical shells subjected to a close-in explosion was performed. The stand-off distance was 12 inches from one end plate. The overall

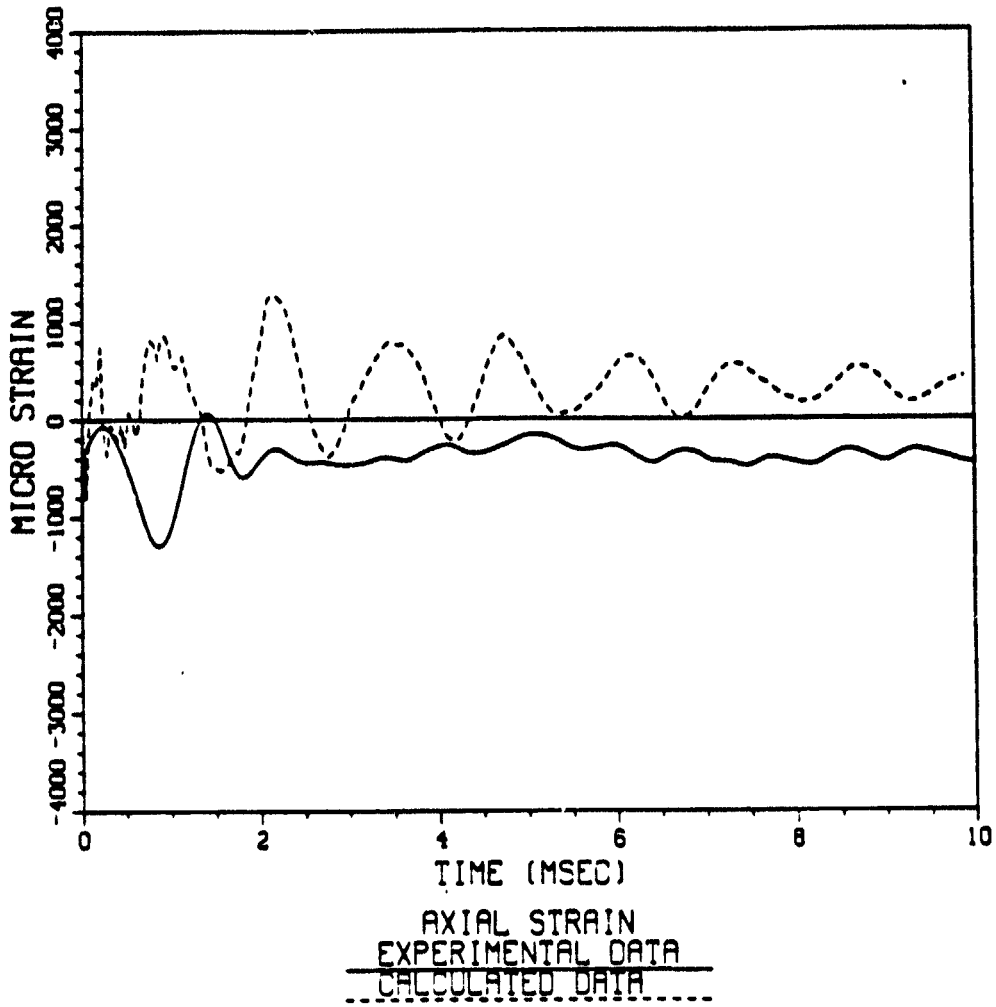
TEST 1, LOCATION A1L



A1L Strain Gage Location (See Figure 2.9)

Figure 3.13. Measured and computed longitudinal strains at 38.5 inches from closest end plate to explosive

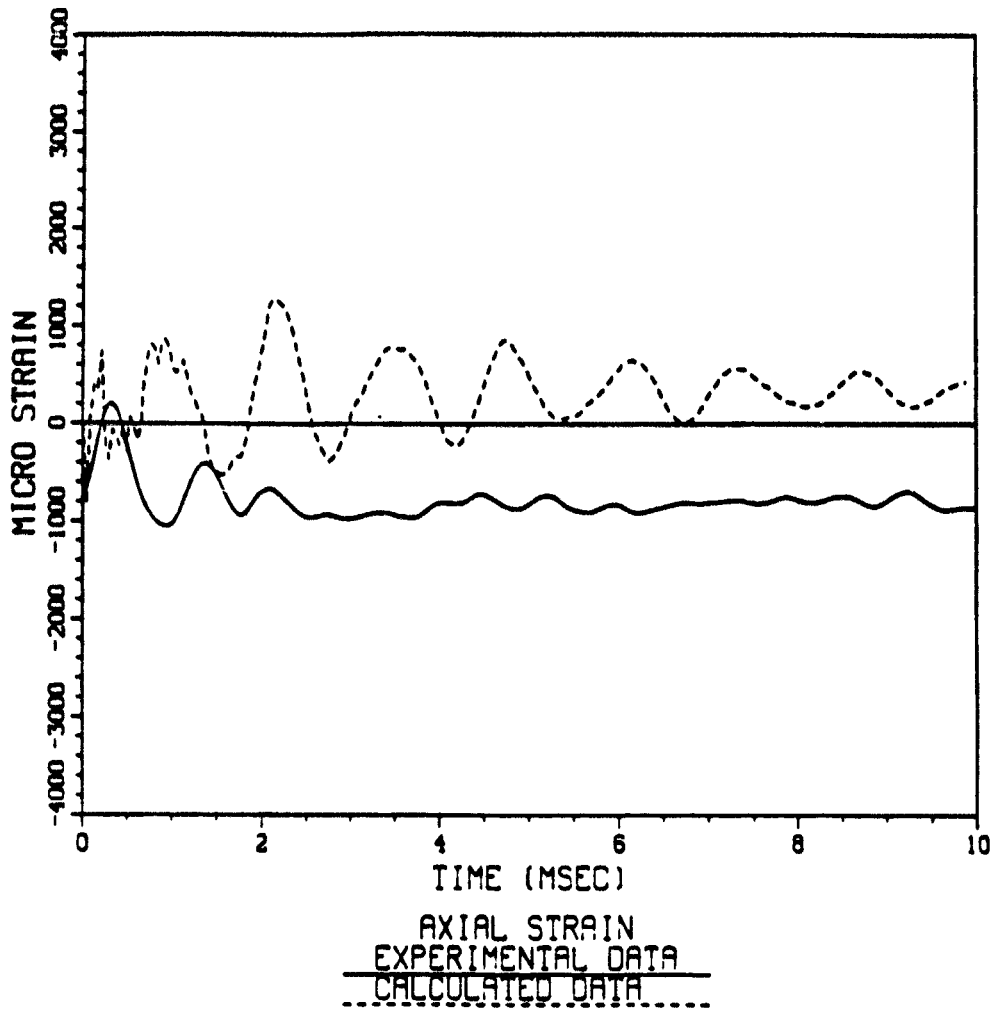
TEST 1, LOCATION C1L



(a) C1L Strain Gage Location (See Figure 2.9)

**Figure 3.14. Measured and Computed Longitudinal Strains at 4.5 Inches from Closest End Plate to Explosive**

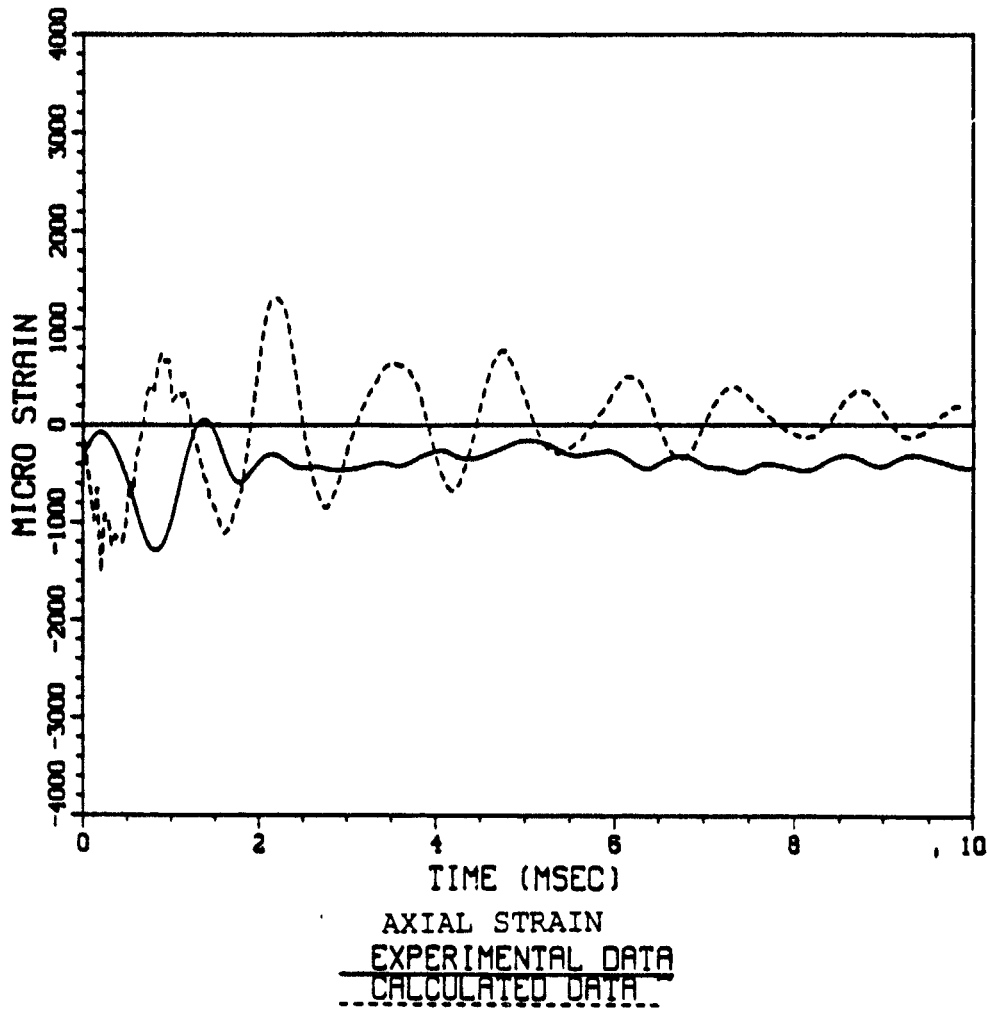
TEST 1, LOCATION C3L



(b) C3L Strain Gage Location (See Figure 2.9)

Figure 3.14. (cont.) Measured and Computed Longitudinal Strains at 4.5 Inches from Closest End Plate to Explosive

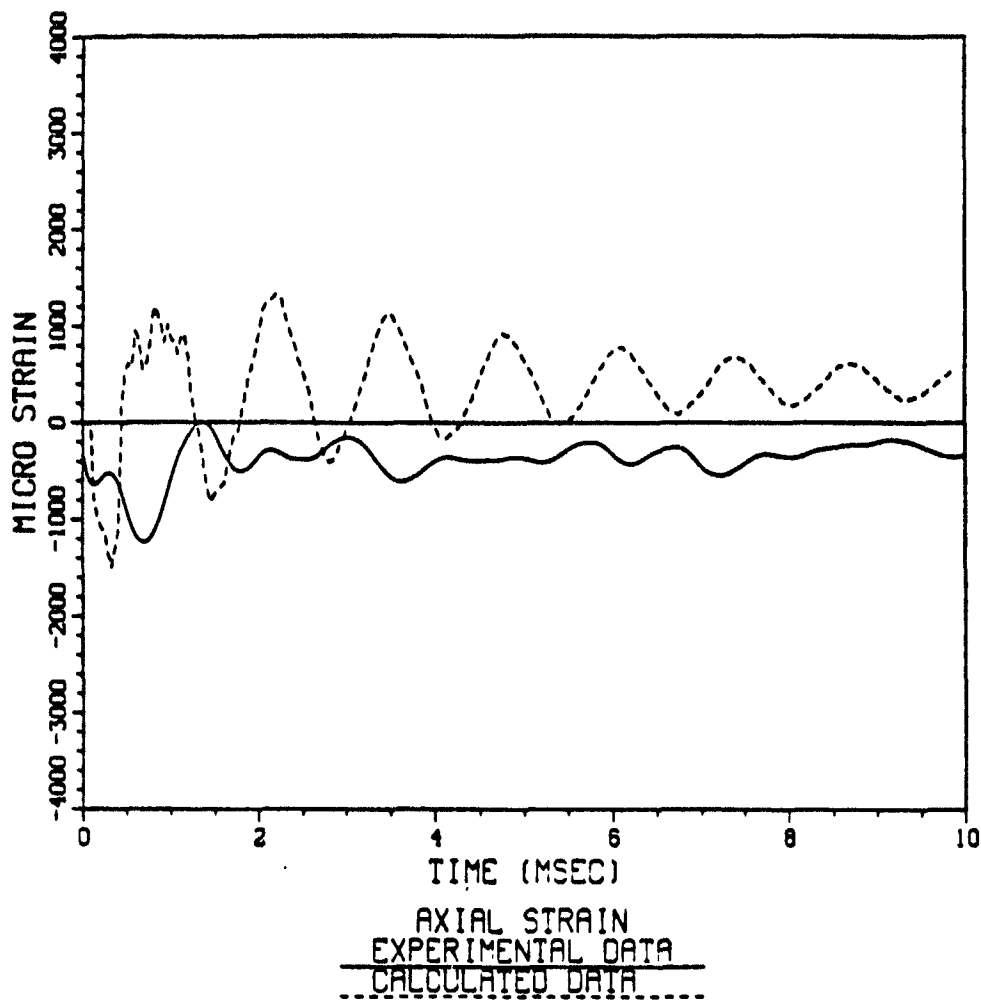
TEST 1, LOCATION C1L



C1L Strain Gage Location (See Figure 2.9)

Figure 3.15. Measured and Computed Longitudinal Strains at 3.5 Inches from Closest End Plate to Explosive

TEST 1, LOCATION B2L



B2L Strain Gage Location (See Figure 2.9)

**Figure 3.16. Measured and Computed Longitudinal Strains at 20.75 Inches from Closest End Plate to Explosive**

geometry with finite element meshes is shown in Figure 2.1. A two pound explosive charge of pentolite was used in the numerical study. The dimension of the cylinder was the same as for the far-field explosion except for a length of 43 inches instead of 42 inches long and the addition of ring stiffeners.

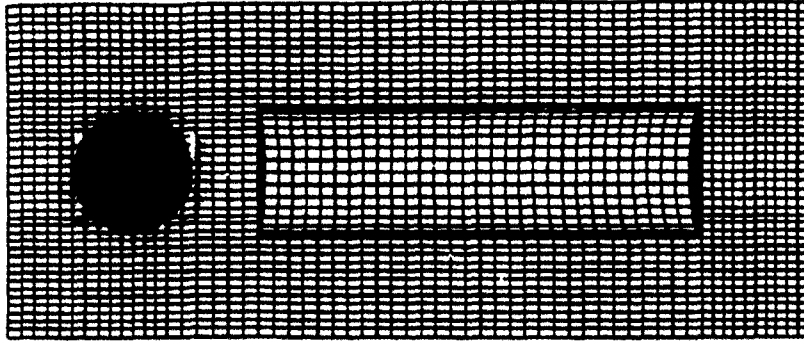
### **1. Pressure Wave Study**

The explosive charge was refined in the numerical model to avoid discontinuities of the sphere as it expanded with time. The pressure wave propagated spherically through the finite element mesh as shown in Figure 3.17.

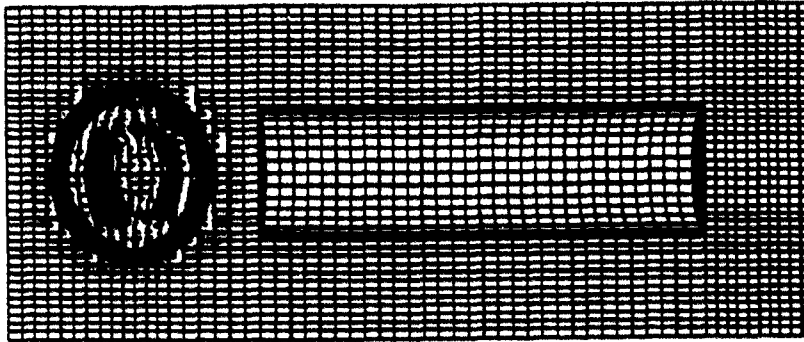
The wave propagation was studied especially at the first interaction between the pressure wave and one end plate. The cylinder was accelerated when the wave first interacted with the end plate. At about 0.3 milliseconds the fluid and end plate velocities break away for a short period. The fluid velocity was lower than that for the shell. Consequently, tension would be induced in the fluid but since fluids cannot experience tension, the water particles break away creating a vacuum. This effect, known as hull cavitation, can be observed in Figure 3.18.

### **2. Ring Stiffener Study**

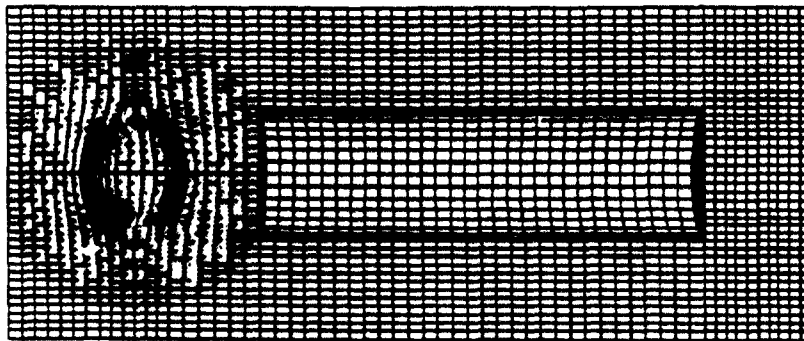
The three cylinders studied were an unstiffened cylinder, a one-ring stiffener cylinder, and a two-ring stiffened cylinder. The ring stiffeners were located at equal intervals between the end plates. In other words, one ring



(a) time = .39420E+02  $\mu$ s

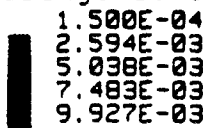


(b) time = .79280E+02  $\mu$ s



(c) time = .11954E+03  $\mu$ s

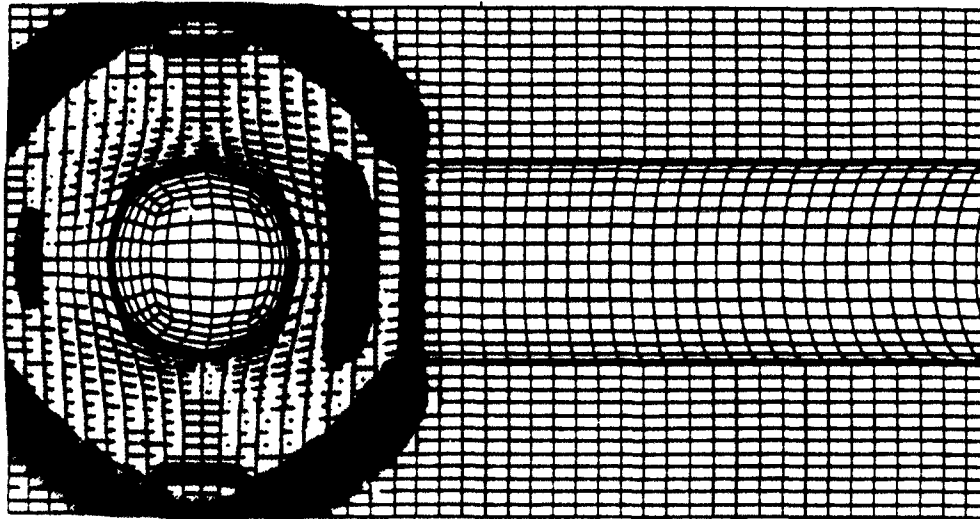
fringe level



1.500E-04  
 2.594E-03  
 5.038E-03  
 7.483E-03  
 9.927E-03

pressure units (g/cm\*\*3 microsec\*\*#2)

**Figure 3.17. Pressure Wave Propagation History in Near-Field Explosion Model**



time = .19984E+03  $\mu$ s

pressure units (g/cm\*\*3 microsec\*\*2)

fringe levels



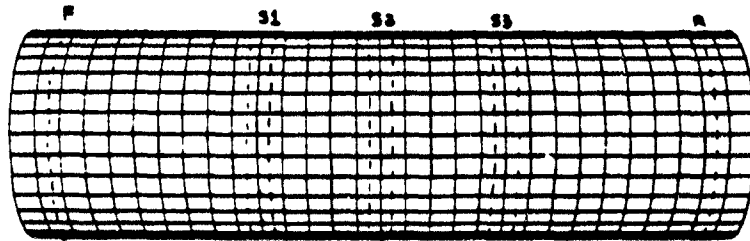
**Figure 3.18. Cavitation at End Plate Closest to Near-Field Explosion**

stiffener was placed at the center of the cylinder as seen previously in Figure 2.2a and the two ring stiffeners were placed at one third distances from the end plates respectively as seen previously in Figure 2.2b. The stiffeners were one inch high and 0.25 inches thick. The nominal material property data of a 6061-T6 Aluminum alloy was used for this study.

The ring stiffened cylinders were compared to the unstiffened cylinder to provide insight into the effectiveness of the ring stiffeners in affecting stress wave propagation and deformation of cylinders. The numerical model was labeled in specific locations where the dynamic response was of interest. These locations are indicated in Figure 3.19 and they include the largely deformed area at the front end of the cylinder, F, the stiffener locations: S1, S2, and S3, and the location close to the remote end plate, R.

The initial shock pressure produced a severe local deformation about three inches from the front end plate for all three cases of cylinders as shown in Figure 3.20. The cylinder yielded identically in all cases because the stiffeners had no effect on the initial deformations near the front end plate until the pressure wave passed through the stiffeners. Comparison of the circumferential strains at location S1 between the unstiffened and two-stiffener models was given in Figure 3.21. In the figure legends A and B denoted shell elements located just before and after the stiffener. The stiffener reduced the compressive peak strain

charge

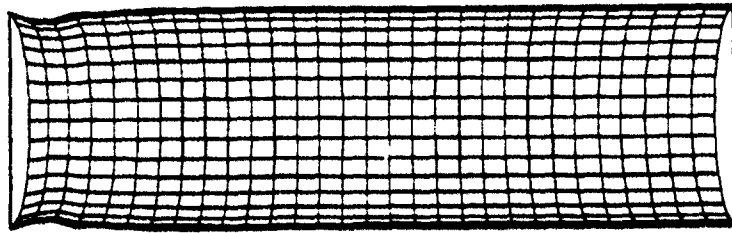


- F: 2.6 inches from end-plate closest to charge
- S1: First stiffener of two-stiffener model
- S2: Stiffener of one-stiffener model
- S3: Second stiffener of two-stiffener model
- R: 40.4 inches from end-plate closest to charge

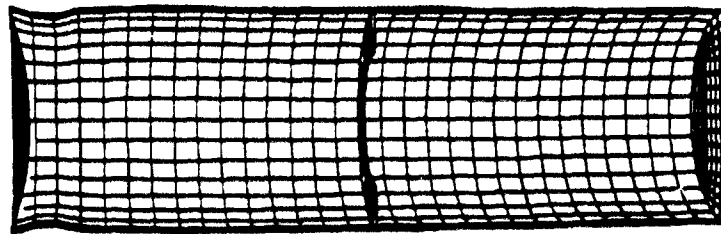
**Figure 3.19. Near-Field Model Locations Chosen for Analysis**

at the location of the stiffener as expected. However, the unstiffened cylinder had a larger relief of the compressive strain than the two-stiffened cylinder. Comparing the same at location S3 indicated that the stiffener not only reduced the compressive peak strain, but also relieved the strain more at later times as shown in Figure 3.22. The circumferential strains at the two stiffeners were plotted in Figure 3.23. The front stiffener had a much larger strain than the back stiffener. The large plastic strain at the front stiffener restrained the recovery of the circumferential strain at the adjacent shell elements at later times compared to the unstiffened cylinder as shown in Figure 3.22.

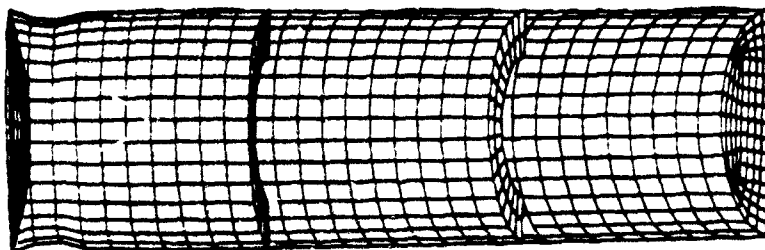
Comparison of the unstiffened and one-stiffener cylinders revealed that the stiffener caused a large relief of the circumferential strain. The center stiffener also caused a big difference in the circumferential strains between the shell elements just before and after the stiffener. The strain was greatly reduced after the stiffener as seen in Figure 3.24. The longitudinal strains were compared in Figures 3.25 and 3.26 between two-stiffened and unstiffened. Figure 3.25 was the comparison at location S1 and Figure 3.26 at location S3. The ring stiffener at location S1 altered the longitudinal strain before and after the stiffener as shown in Figure 3.25. The stiffener at location S1 induced a higher longitudinal strain at the shell element located just before the stiffener compared to that at the same location of the unstiffened



(a) Unstiffened model



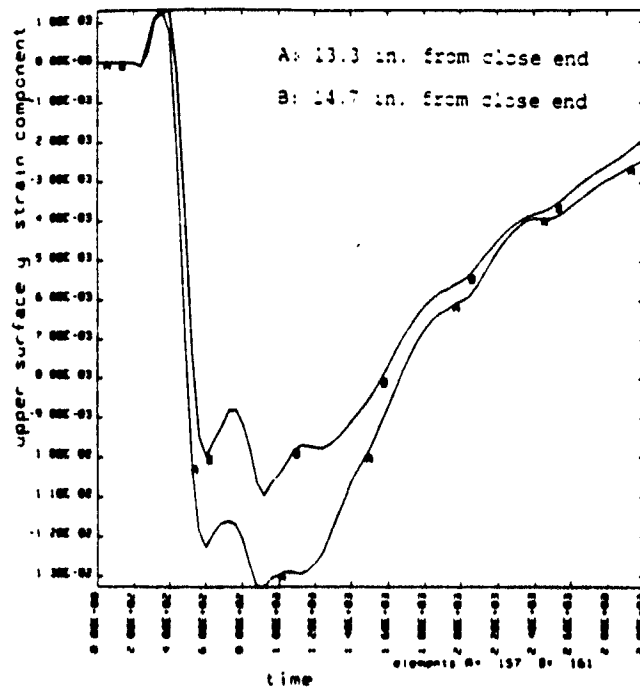
(b) One-stiffener model



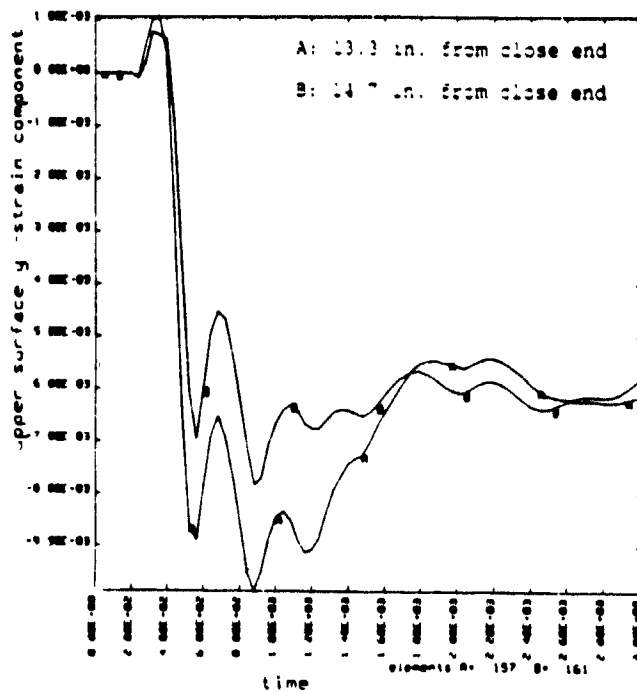
(c) Two-stiffener model

time = .35999E+03  $\mu$ s

Figure 3.20. Local Deformations for Near-Field Models

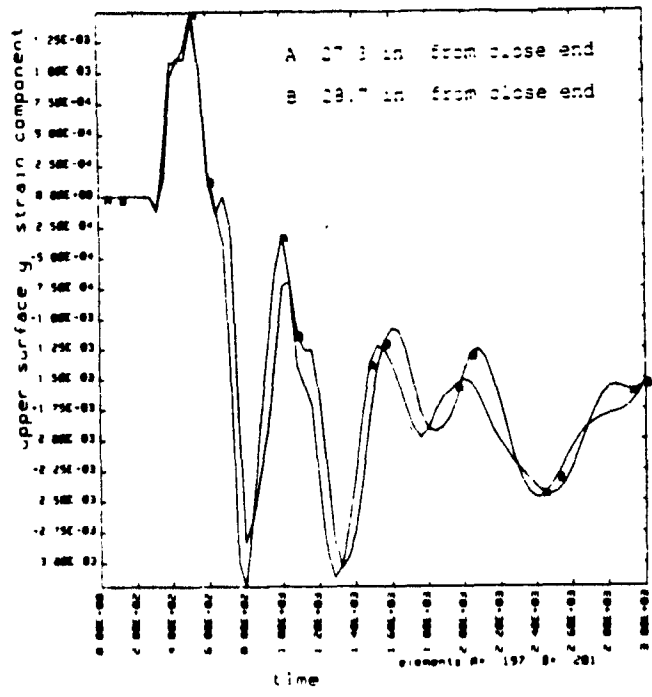


(a) Unstiffened model

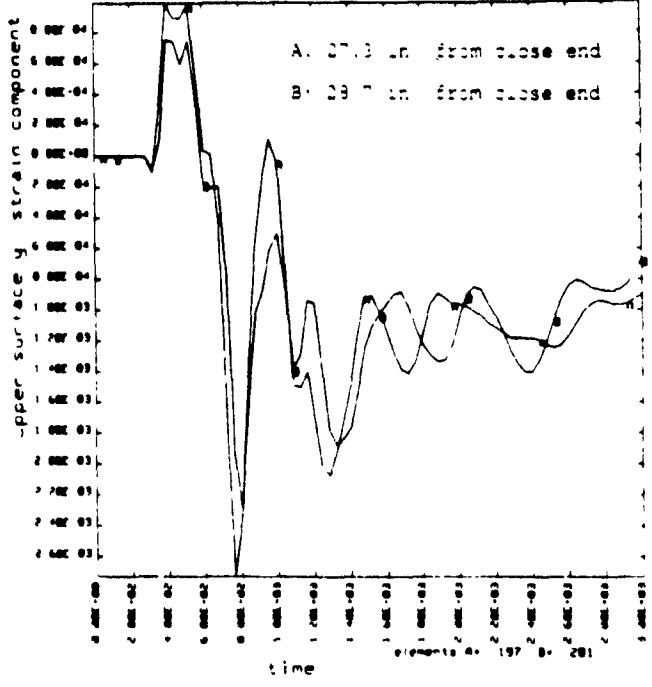


(b) One-stiffener model

Figure 3.21. Circumferential Strains at Both Sides of Stiffener Closest to Explosive Charge

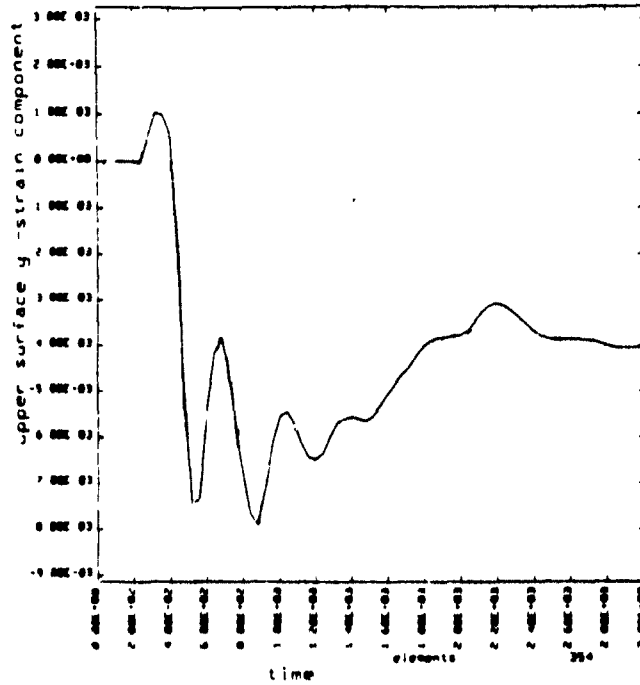


(a) Unstiffened model

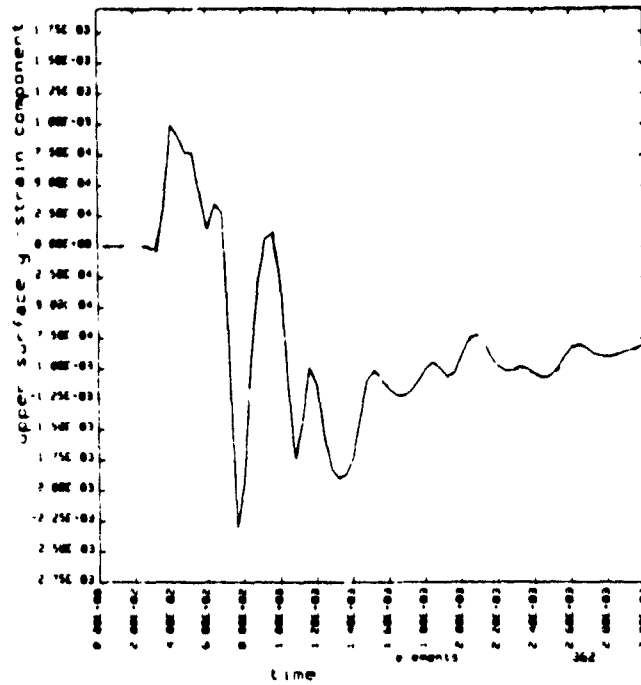


(b) One-stiffener model

Figure 3.22. Circumferential Strains at Both Sides of Stiffener Farthest from Explosive Charge



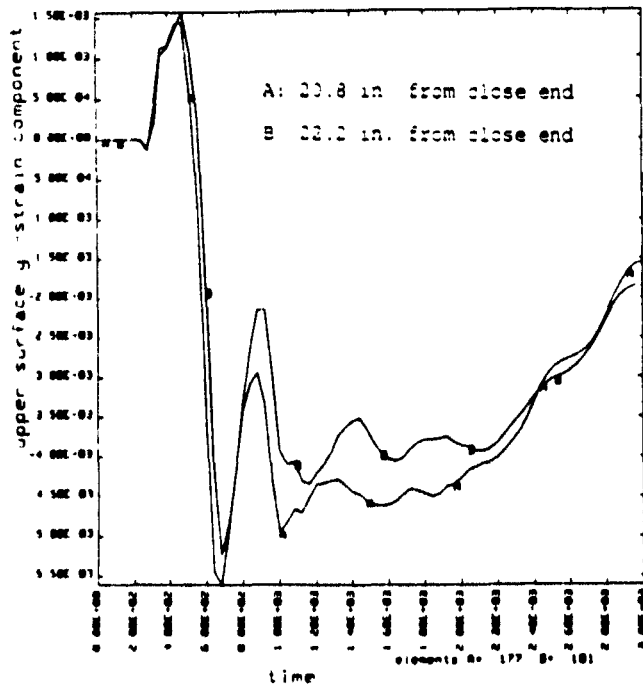
(a) Stiffener 14.5 in. from end close to explosive



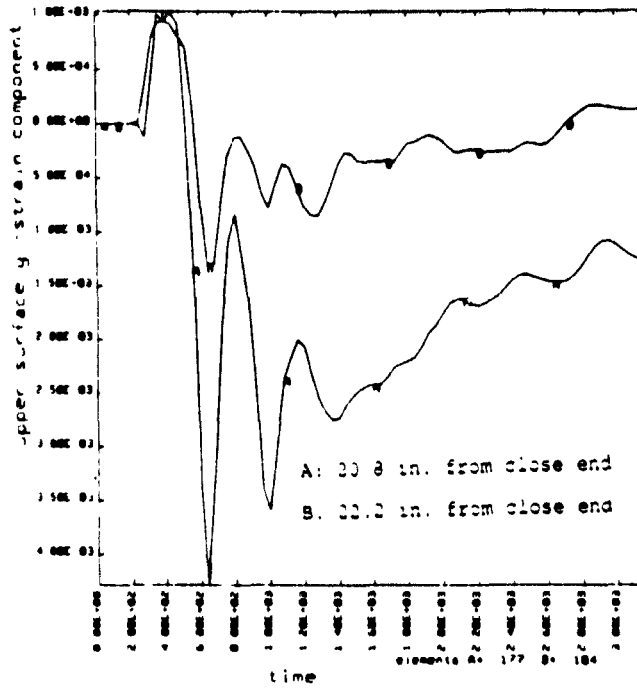
(b) Stiffener 28.5 in. from end close to explosive

**Figure 3.23. Circumferential Strains at Both Stiffeners of Two-Stiffener Model**

cylinder. In addition, the stiffener relieved the strain near to zero at the shell element located just after the stiffener as time elapsed. The effect of the stiffener at location S3 on the longitudinal strain was much smaller compared to that at location S1. No accordion mode was observed for all three cases of cylinders.

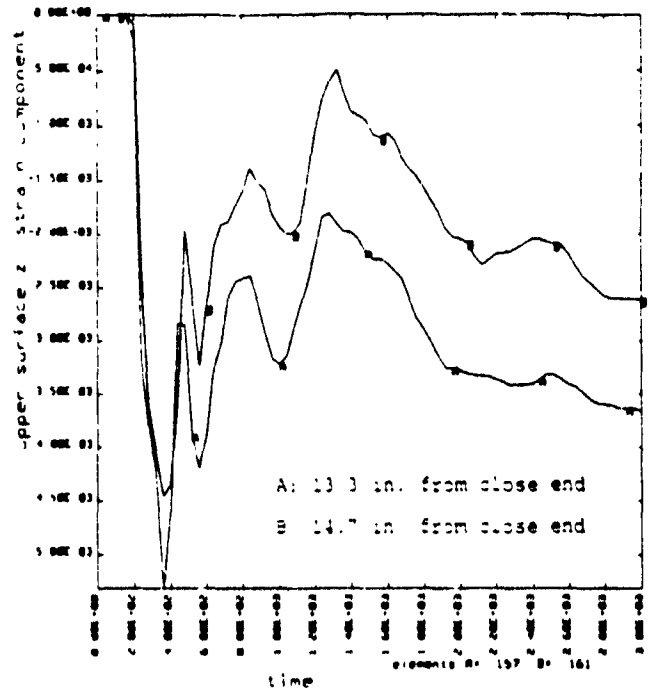


(a) Unstiffened model

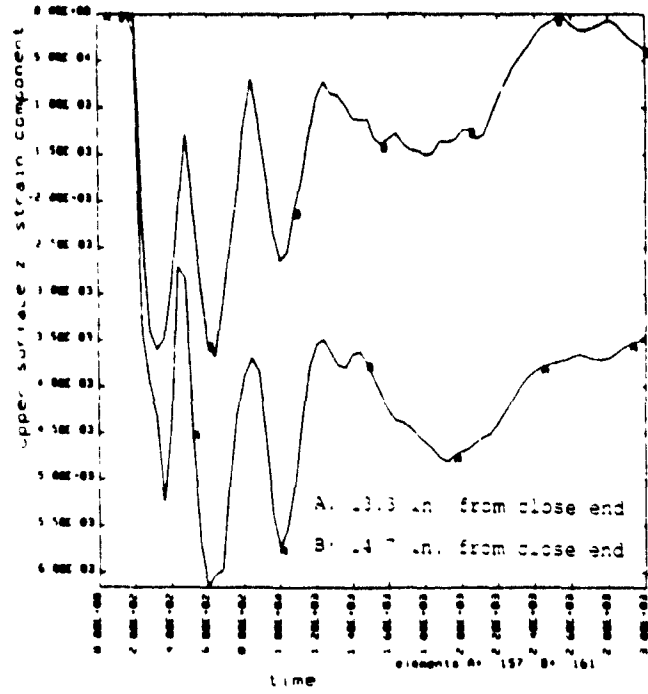


(b) One-stiffener model

Figure 3.24. Circumferential Strain Comparison for Unstiffened and One-Stiffener Models

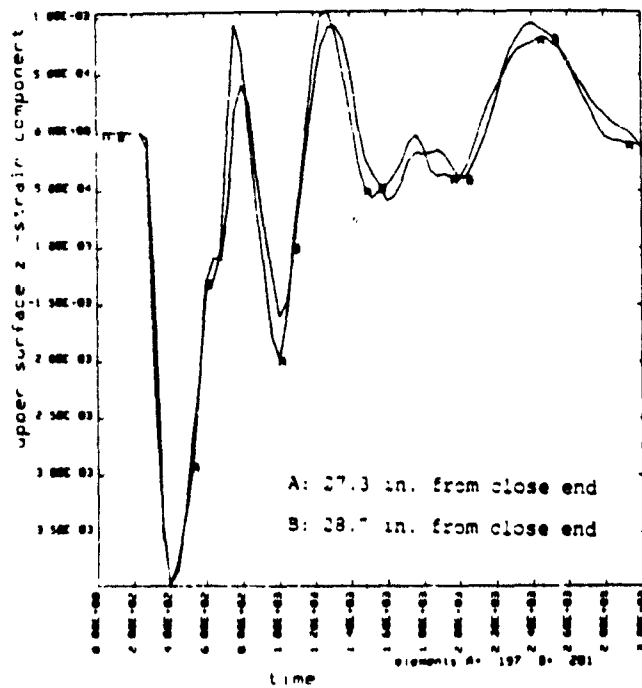


(a) Unstiffened model

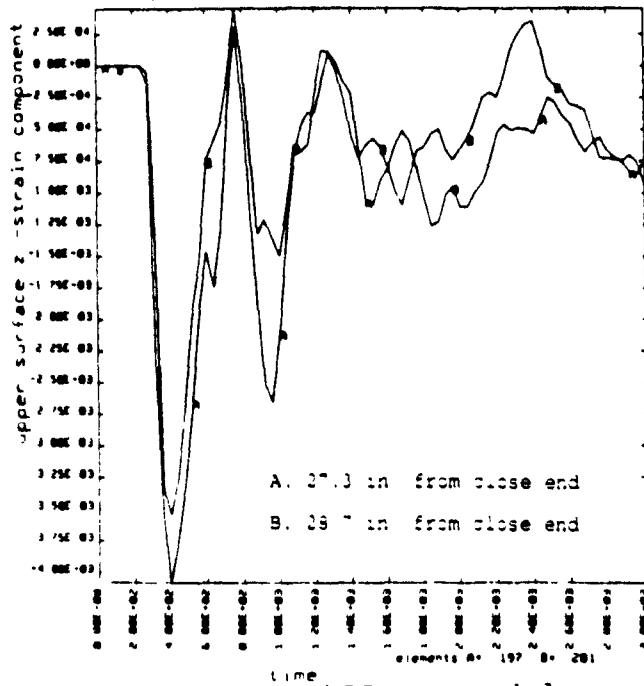


(b) Two-stiffener model

Figure 3.25. Longitudinal Strains (Unstiffened and Two-Stiffened) at Stiffener Location Closest to Charge



(a) Unstiffened model



(b) Two-stiffener model

**Figure 3.26. Longitudinal Strains (Unstiffened and Two-Stiffened) at Stiffener Location Far from Charge**

#### IV. CONCLUSIONS

The numerical and experimental study was performed to investigate the nonlinear dynamic response of cylindrical shells to end-on explosions. Unstiffened and ring-stiffened cylinders capped at both ends were subjected to near-field and far-field explosions. Both finite element and boundary element methods were used for the numerical study. The experiment was fulfilled using a 6061-T6 aluminum alloy cylinder and a sixty pound HBX charge with 28 feet stand-off distance.

The far-field explosion resulted in a nearly symmetric deformed shape of the cylinder about the center plane between the two end plates, while the near-field explosion caused very unsymmetric deformation about the center plane. Both far-field and near-field explosions induced localized deformations near the end plates. The localized deformations were located close to both end plates for the far-field explosion and a very severe, localized deformation occurred close to the closest end plate to the explosive charge for the near-field explosion regardless of the existence of ring stiffeners. The accordion mode was observed for the cylinder subjected to the far-field explosion but not for the cylinders subjected to near-field explosion.

A parametric study was undertaken to examine the effect of end plates on the deformation of the cylinder subject to the

far-field explosion. A variation of the density and stiffness of the end plates caused a significant change in the stress wave propagation and the deformation of the cylinder. However, the change of stiffness had more significant effects than the change of density.

The circumferential strains under the far-field explosion had large initial compressive peaks and returned to the steady state values quickly. The circumferential strains were larger near the end plates than around the center due to the local deformation. The localized deformations were caused by the compressive shock pressure applied on the end plates. The longitudinal strains under the far-field explosion were compressive at the shell near the end plate closer to the charge but tensile at the opposite location.

The failure of pressure and several strain gages prevented a quantitative comparison between the numerical and experimental results. A qualitative comparison was possible between the two solutions only at a few locations. The comparison was better near the remote end plate than the near end plate to the charge. A good explanation for this discrepancy was not possible due to the lack of information in the experiment. However, this was the first test among a series of experiments to be performed. More detailed information from the next tests may provide a better understanding of the discrepancy.

The effect of ring stiffeners was larger on the circumferential strain than on the longitudinal strain. The ring stiffener located close to the severe local deformation had a more pronounced effect on the strains. The ring stiffeners in general reduced the circumferential strain compared to the unstiffened case and stiffeners also gave more recovery of the strain. However, when the stiffeners had a large plastic deformation, they allowed less relief of the circumferential strain.

## **APPENDIX: UNIAXIAL TENSION TEST DATA FOR 6061-T6 ALUMINUM**

A uniaxial tension test was performed on a test specimen of 6061-T6 Aluminum to find its material properties. The specimen was cut to ASTM E8-69 specifications for rectangular tension test specimens.

A Material Test System (MTS) model 810 was used for the test and the gage length was set at two inches for the tensile test. The tensile test was performed at a rate of 400 sec/inch and a load versus displacement curve was plotted as shown in Figure A.1. The MTS model did not have data recording capabilities and therefore, some points were taken from the graph after the test to plot the appropriate stress-strain curve. Some sample data points are listed in Table A.1.

From the stress-strain curve in Figure A.2, the yield stress was found to be close to 43 ksi using a 0.2 percent offset and the modulus of elasticity was 10800 ksi.

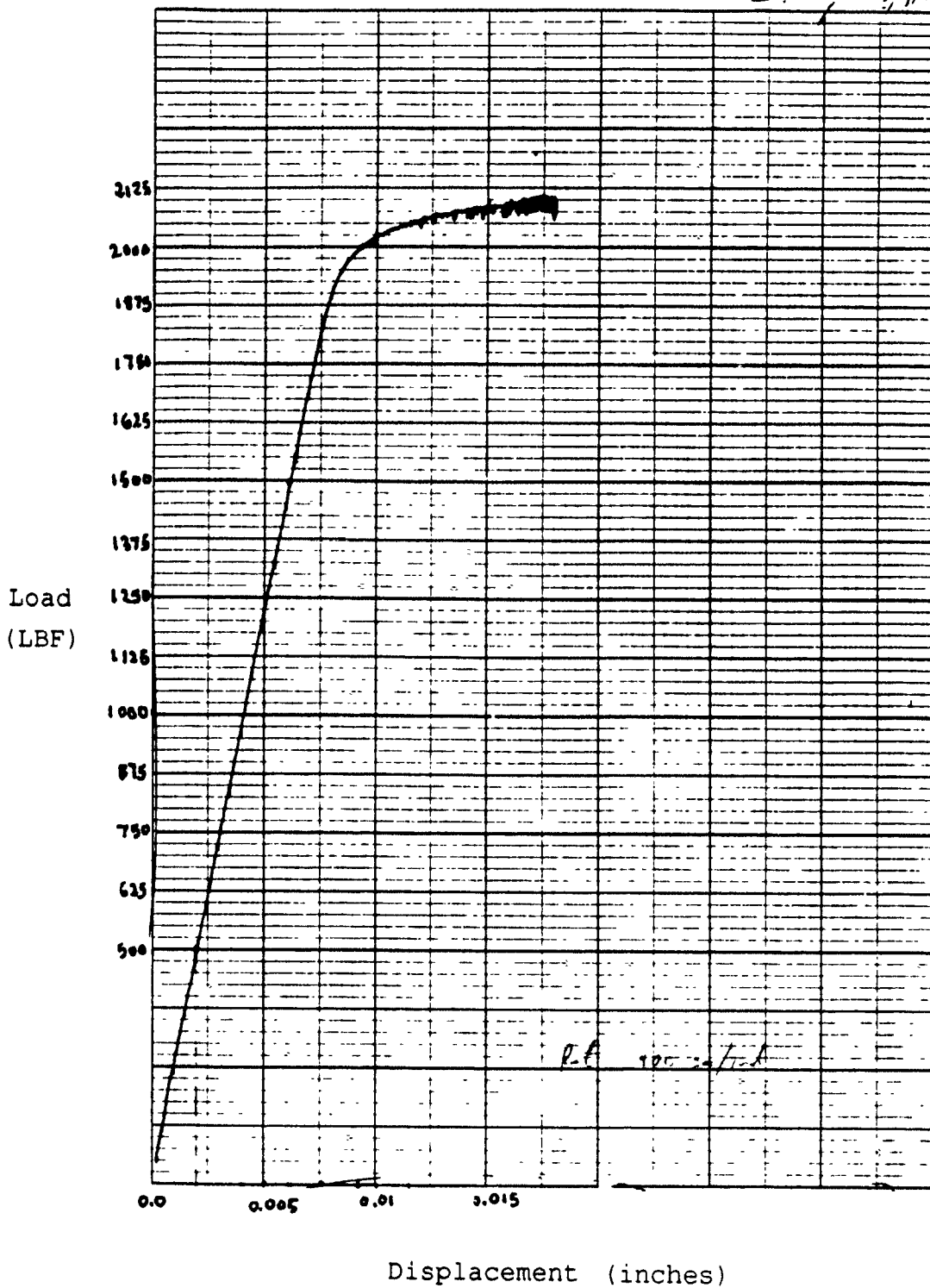
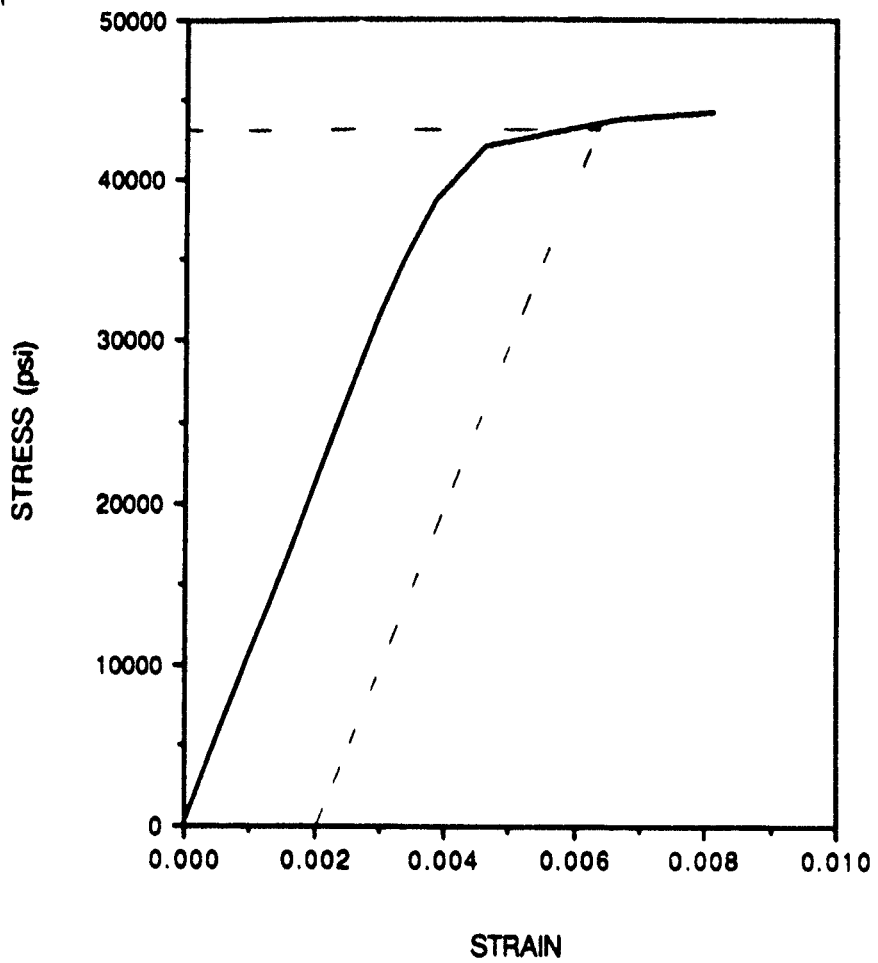


Figure A.1. Load-Displacement Curve for 6061-T6 Aluminum



**Figure A.2. Stress-Strain Curve for 6061-T6 Aluminum**

**TABLE A.1**

LOAD (LBF)	STRESS (psi)	STRAIN
0.0	0.0	0.0
500	10526	0.0010
625	13158	0.00125
1000	21053	0.0020
1250	26316	0.0025
1500	31579	0.003125
1625	34211	0.003375
1750	36842	0.003625
1875	39474	0.003875
2000	42105	0.004625
2075	43684	0.006625
2100	44210	0.008125

## LIST OF REFERENCES

1. Budweg, H.L. and Shin, Y.S., "Experimental Studies on the Tripping Behavior of Narrow T-Stiffened Flat Plates to Hydrostatic Pressure and Underwater Shock," *Proceedings of the 58th Shock and Vibration Symposium*, Vol. 1, NASA Publication 2488, pp. 61-95, October 1987.
2. Jones, R.A., and Shin, Y.S., "The Response and Failure Mechanisms of Circular Metal and Composite Plates Subjected to Underwater Shock Loading," *Proceedings of the 61st Shock and Vibration Symposium*, Vol. 3, Pasadena, California, pp. 163-178, October 16-18, 1990.
3. Kwon, Y.W., Fox, P.K., and Shin, Y.S., "Response of a Cylindrical Shell Subject to a Near Field Side-On Explosion," *Proceedings of the 62nd Shock and Vibration Symposium*, v.2, pp. 483-492, 29-31 October 1991.
4. Banerjee, P.K., and Butterfield, R., *Boundary Element Methods in Engineering Science*, McGraw Hill Book Company (UK) Limited, London, 1981.
5. Stillman, D.W., and Hallquist, J.O., *VEC/DYNA3D User's Manual (Nonlinear Dynamic Analysis of Structures in Three Dimensions)*, Software Technology Corporation, 1990.
6. DeRuntz, J.A., and Rankin, C.C., *Applications of the USA and USA-STAGS Codes to Underwater Shock Problems*, v.1, v.2, Palo Alto, California, 1990.
7. Geers, T.L., "Computational Methods for Transient Analysis," *Boundary-Element Methods for Transient Response*, Elsevier Science Publishers, p. 231, 1983.
8. Hallquist, J.O., *LS-TAURUS An Interactive Post-Processor for the Analysis Codes LS-NIKE3D, LS-DYNA3D, and TOPAZ3D*, Livermore Software Technology Corporation, 1990.
9. Stillman, D.W., and Hallquist, J.O., *LS-INGRID A Pre-Processor And Three Dimensional Mesh Generator for the Programs LS-DYNA3D, LS-NIKE3D and TOPAZ3D*, Livermore Software Technology Corporation, 1991.

10. Dobratz, B.M., *LLNL Explosives Handbook*, Lawrence Livermore Laboratory, University of California, p. 8-21, 1981.
11. Askeland, D.R., *The Science and Engineering of Materials, Second Edition*, PWS-KENT Publishing Company, p. 421, 1989.
12. King, F., *Aluminum and its Alloys*, Halsted Press, p. 226, 1987.
13. Timoshenko, S.P., and Gere, J.M., *Theory of Elastic Stability*, McGraw-Hill Book Company, Inc., p. 459, 1961.

## INITIAL DISTRIBUTION LIST

	No. of Copies
1. Defense Technical Information Center Cameron Station Alexandria, Virginia 22304-6145	2
2. Library, Code 52 Naval Postgraduate School Monterey, California 93943-5002	2
3. Professor Y.W. Kwon, Code ME/Kw Department of Mechanical Engineering Naval Postgraduate School Monterey, California 93940	2
4. Professor Y.S. Shin, Code ME/Sg Department of Mechanical Engineering Naval Postgraduate School Monterey, California 93943	1
5. Department Chairman, Code ME Department of Mechanical Engineering Naval Postgraduate School Monterey, California 93940	1
6. Dr. Thomas T. Tsai Defense Nuclear Agency 6801 Telegraph Road Alexandria, Virginia 22310	1
7. Dr. Kent Goering Defense Nuclear Agency 6801 Telegraph Road Alexandria, Virginia 22310	1
8. Mr. Frederick A. Costanzo David Taylor Research Center Underwater Explosion Research Division Norfolk Naval Shipyard, Bldg 369 Portsmouth, Virginia 23709	1

9. Dr. B. Whang, Code 1750.2 1  
Hull Group Head, Submarine Protection Division  
David Taylor Naval Ship Research and Development  
Center  
Bethesda, Maryland 20084-5000
10. Professor Thomas L. Geers 1  
Department of Mechanical Engineering  
Campus Box 427  
University of Colorado  
Boulder, Colorado 80309
11. Dr. John A. DeRuntz Jr. 1  
Computational Mechanics Section  
Lockheed Palo Alto Research Laboratories  
3251 Hanover Street  
Organization 93-30  
Palo Alto, California 94304